AD_____

Award Number: W81XWH-04-1-0551

TITLE: Investigation of Metastatic Breast Tumor Heterogeneity and Progression using Dual Optical/SPECT Imaging

PRINCIPAL INVESTIGATOR: Peter P. Antich, Ph.D.

CONTRACTING ORGANIZATION: University of Texas Southwestern Medical Center
Dallas, TX 75390-9058

REPORT DATE: May 2006

TYPE OF REPORT: Annual

PREPARED FOR: U.S. Army Medical Research and Materiel Command
Fort Detrick, Maryland 21702-5012

DISTRIBUTION STATEMENT: Approved for Public Release;
Distribution Unlimited

The views, opinions and/or findings contained in this report are those of the author(s) and should not be construed as an official Department of the Army position, policy or decision unless so designated by other documentation.

REPORT DOCUMENTATION PAGE

Form Approved
OMB No. 0704-0188

Public reporting burden for this collection of information is estimated to average 1 hour per response, including the time for reviewing instructions, searching existing data sources, gathering and maintaining the data needed, and completing and reviewing this collection of information. Send comments regarding this burden estimate or any other aspect of this collection of information, including suggestions for reducing this burden to Department of Defense, Washington Headquarters Services, Directorate for Information Operations and Reports (0704-0188), 1215 Jefferson Davis Highway, Suite 1204, Arlington, VA 22202-4302. Respondents should be aware that notwithstanding any other provision of law, no person shall be subject to any penalty for failing to comply with a collection of information if it does not display a currently valid OMB control number. **PLEASE DO NOT RETURN YOUR FORM TO THE ABOVE ADDRESS.**

1. REPORT DATE *(DD-MM-YYYY)*	**2. REPORT TYPE**	**3. DATES COVERED** *(From - To)*
01-05-2006	Annual	1 May 2005 - 30 Apr 2006

4. TITLE AND SUBTITLE
Investigation of Metastatic Breast Tumor Heterogeneity and Progression using Dual Optical/SPECT Imaging

5a. CONTRACT NUMBER

5b. GRANT NUMBER
W81XWH-04-1-0551

5c. PROGRAM ELEMENT NUMBER

6. AUTHOR(S)
Peter P. Antich, Ph.D.

E-Mail: Peter.Antich@UTSouthwestern.edu

5d. PROJECT NUMBER

5e. TASK NUMBER

5f. WORK UNIT NUMBER

7. PERFORMING ORGANIZATION NAME(S) AND ADDRESS(ES)
University of Texas Southwestern Medical Center
Dallas, TX 75390-9058

8. PERFORMING ORGANIZATION REPORT NUMBER

9. SPONSORING / MONITORING AGENCY NAME(S) AND ADDRESS(ES)
U.S. Army Medical Research and Materiel Command
Fort Detrick, Maryland 21702-5012

10. SPONSOR/MONITOR'S ACRONYM(S)

11. SPONSOR/MONITOR'S REPORT NUMBER(S)

12. DISTRIBUTION / AVAILABILITY STATEMENT
Approved for Public Release; Distribution Unlimited

13. SUPPLEMENTARY NOTES

14. ABSTRACT:

This clinical nurse research award builds directly on the principal investigator's extensive clinical background in women's health and primary care by facilitating her transition from geriatric research to breast cancer research. The overall purpose of this award is to provide training for the development of a career in breast cancer research. The proposed training plan will lead to advanced skills in research design, data management and analysis and in working with interdisciplinary research teams to improve outcomes of care of patients with breast cancer. The purpose of the research is to (1) describe NCF in women undergoing chemotherapy and in those undergoing surgically-induced menopause; (2) identify changes in NCF over time; (3) describe nature, severity, onset, duration, persistence of changes; (4) identify relationship between NCF and chemotherapy, menopause, symptom distress and functional status.

15. SUBJECT TERMS
SPECT, Optical Bioluminescence Imaging, Metastatic Development, Tumor Heterogeneity

16. SECURITY CLASSIFICATION OF:			**17. LIMITATION OF ABSTRACT**	**18. NUMBER OF PAGES**	**19a. NAME OF RESPONSIBLE PERSON**
a. REPORT	**b. ABSTRACT**	**c. THIS PAGE**			USAMRMC
U	U	U	UU	49	**19b. TELEPHONE NUMBER** *(include area code)*

Standard Form 298 (Rev. 8-98)
Prescribed by ANSI Std. Z39.18

Table of Contents

Cover……

SF 298……2

Introduction……...4

Body……4

Key Research Accomplishments……9

Reportable Outcomes……9

Conclusions……10

Appendices……11

INTRODUCTION

We have made substantial progress in our techniques for the detection of metastases. We have demonstrated our capability to detect millimeter or sub-millimeter metastases in mice by light emission. To this end we have used Light Emission Tomography (LET), a technique based on bioluminescence of cancer cells infected with luciferase, to detect metastases in the lung and head. We have begun assessment of perfusion using fluorescence imaging. In addition, our technological focus is on the simultaneous use of Single-photon Emission Computed Tomography (SPECT), and to this end we have developed a new form of micro-SPECT based on cooled, electron-multiplied Charge-Coupled Devices (EMCCDs) fwith which we are performing ongoing imaging experiments. We have also collaborated on the assessment of a new, promising SPECT imaging agent, clioquinol or Iodinated hydroxyquinoline. We will use bioluminescence imaging to test if clioquinol imaging detects areas where tumor cells proliferate and establish metastases and to identify the relative times at which the images first appear.

BODY

Light Emission Tomography.
We have tested various sites within the body to determine the circumstances under which we could reliably detect metastases. We developed means to calibrate light intensity in terms of photons/unit area/sec and to evaluate the light intensity emitted by the different cell lines used in our studies. We were able to detect in vitro with the same instrument extended distributions with 500 cells and foci estimated at 10-30 cells when the cells had sufficient emission intensities. We then undertook imaging studies of metastases. To investigate a biological model of breast cancer metastasis to the lung, 10^6 MDA MB 231-Luc cells were injected into the tail vein of a nude mouse. We performed sequential images of the animal both by LET and by MRI. Metastases were unambiguously identified 22 days post-injection as three separate nodules in the two lungs; and the two larger foci in the left lung were confirmed by MRI on day 46.

The figure shows four 1mm-thick tomographic slices, 2 for LET and 2 for MRI. LET shows three metastases on days 22 and 43, two in the left and one in the right lung. Using a 4.5 T small animal magnet, MRI confirms the two metastases in the left lung on day 46. In the LET images the maximum intensity of light emission increases by a factor of 3-3.5 between days 22 and 32.

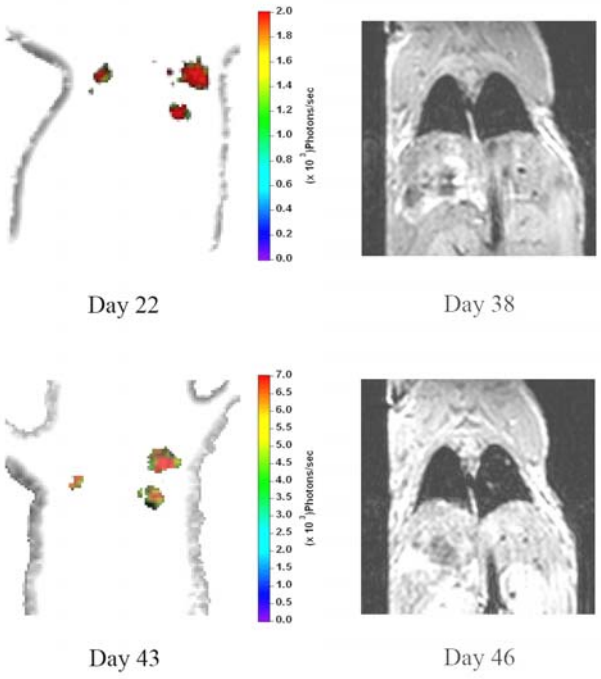

We then investigated whether or not the device could image small tumors in the cranial cavity. $8x10^3$ tumor cells were injected at two sites, within the cranial cavity of a nude mouse and in the flank, $5x10^3$ in the head of a second mouse and tumors were allowed to develop freely. The tumors grew at a slow rate and displayed similar light intensity at early times, diverging only slightly in their growth pattern. Thus, brain metastases are also detectable.

Day 0 Injected cells 8,000 Injected cells 5,000

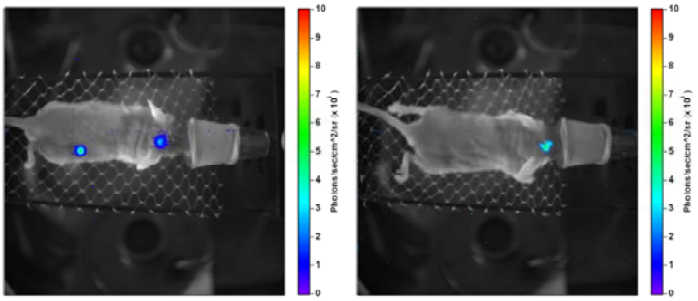

DAY 11

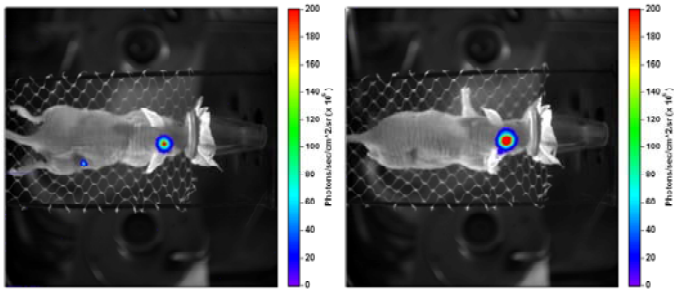

As the tumors developed between day 0 and 11, the light intensity increased 20-fold. To study smaller foci and number of cells it is necessary to adopt higher magnification optics. We are investigating means to do so. By way of comparison, an MRI image at 4.75 T shows the central location of the tumor in the T1 contrast image at day 10.

MDA-MB231 in brain on day10 of (8000 cells; with flank tumor)

T1-weighted

T2-weighted

T1 contrast

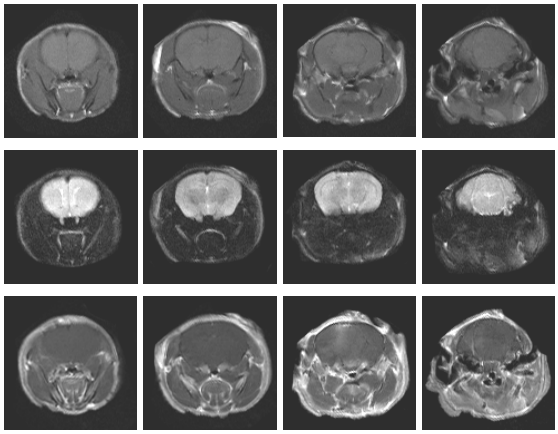

MicroSPECT

Our project proposed to test multimodality imaging, joining LET and SPECT (Single Photon Emission Tomography). To this end we have developed a camera equipped with electron multiplying CCDs. The CCDs are coupled to scintillating crystals after passing through a collimator and detect the interactions of gamma rays with the crystal. Integrating these signals over time produces images used for SPECT reconstruction.

The use of integration in ccdSPECT is complicated by two factors. First, the integration of the stochastic scintillation light leads to deceased signal to noise compared to photon counting. Fortunately for scintillatiors such as CsI(Tl) this effect is only on the order of 10%. Second, there is a four-fold resolution penalty for energy-integrating CCD gamma cameras. As we previously demonstrated, the intrinsic resolution of our CCD gamma camera is slightly less than 400 micrometers. On the other hand, others have reported that resolutions below 100 micrometers are possible with CCD-based gamma cameras in photon counting mode.

To investigate possible integration of photon counting into our dual modality imaging system, we have developed a low cost camera based on the cheapest electron-multiplication CCD on the market (the Texas Instruments TC253). In addition, we have also evaluated more costly commercial systems (Princeton Instruments/Acton PhotonMax 512B and the Andor Luca). Additional sensitivity was accomplished by reducing the field-of-view of the camera. Because the optical transport of scintillation light is related to the field-of-view by a quadratic, reducing the FOV by a factor of 4-5 leads to 16-25 times more photons reaching the CCD.

The Texas Instruments TC253 is a VGA-format Impactron sensor with electron multiplication gain up to 1000. The sensor is cooled with a 3 stage Peltier system. Although rated at -10 C, we have successfully operated the TC253 at -42 C. The interface to the sensor consists of analog line drivers controlled digitally by a commercial field programmable gate array (FPGA – National Instruments PCI-4312). Software for clocking the CCD was developed in house using National Instruments LabVIEW. Extensive testing in dark reveals that the TC253 is sensitive to single electrons. Unfortunately, an unspecified characteristic of this chip is a relatively large spurious charge (2-4 electrons per pixel). Because this charge is also multiplied by the multiplication registers, it effectively blinds the camera to the faintest flashes of light.
We do however envision that the TC253 camera will make an effective integration camera, and efforts are underway to completely eliminate all dark current through more cooling. A 2nd generation TI Impactron chip (TC247) is available with lower spurious transfer charge and would essentially be a drop-in replacement for the TC253, although at 6 times the cost. This sensor has been evaluated in a commercial camera as described below.

The Princeton Instruments/Acton PhotonMax 512B is a top-of-line back illuminated emCCD camera. This camera incorporated the e2v CCD 97 sensor. Using this camera, we have successfully implemented photon counting at 30 frames per second with both cobalt-57 and iodine-125. Surprisingly, photon counting was possible for >100 keV gammas without electron multiplication, using the traditional readout port of the sensor (7 electron read noise). We have also evaluated the Andor Luca, a budget emCCD camera based on the TI TC247 front illuminated interline sensor. The camera was also effective at photon counting,

although data collection speed was reduced due to the computer interface (USB versus CameraLink).

For a system with 10-20 CCD-based gamma cameras, which could be designed for very fast imaging of the breast and axilla, it is evident that the cost per camera must be below $5000. This obviously rules out the most expensive emCCD offerings. In the coming years, however, CCD cameras with sub-4 electron read noise may be cheap enough to consider such a system. However, since multiple video streams will yield immense data rates, effective data acquisition will need to be addressed. This is the focus of our research.

We have tested the ability of the highest-sensitivity CCD camera currently available to detect not only an integrated signal but also single-gamma-ray interactions. The appended movie (CD) shows the detection of multiple, single photon events, as the source is moved away from the crystal (single photon events disappear) or near it (multiple events).

We note that if the LET camera is used to detect the skin of the animal and the SPECT camera is used simultaneously, the perception of the distribution is significantly improved. In the figure below, the MDDP distribution identifies the skeleton. This is also true of X-ray imaging, where CT and PET nor SPECT can be used together.

FLUORESCENCE IMAGING.

We note that in addition we can merge bioluminescence with fluorescence imaging. If a dextran tagged with Alexa Flours is injected in a mouse illuminated in white light, the autofluorescence presents a background signal 14 times lower than the signal produced by the fluor. In the whole body image the prominent light source is the heart as the polymer remains in the vasculature

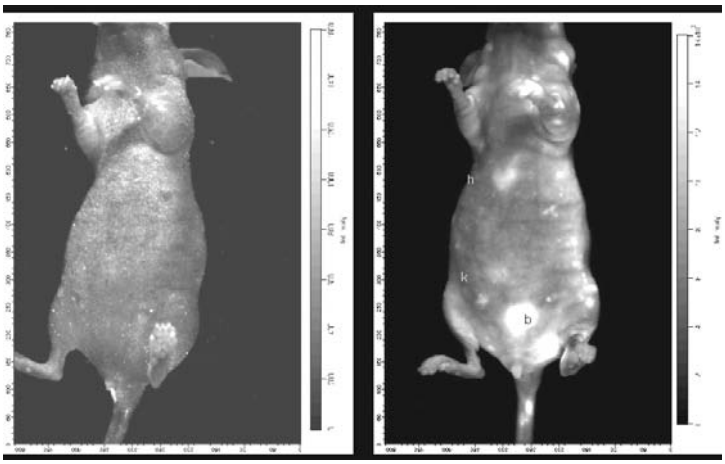

The left habd side image shows the pre-injection mouse, the one at right was acquired 3 min PI. Heart, kidney and bladder are the highest intensity sources (note that the kidney is seen through the mouse body in this ventral view).
If the same agent is injected in a mouse in which an MDA-MB231 breast cancer tumor grows in the mammary fat pad, a whole body image shows anatomic details as well as the tumor; a higher magnification image reveals the viable tumor against a darker halo around the tumor, produced by absorption of the light used to induce fluorescence by blood vessels and by a dense population of extravasated red blood cells.

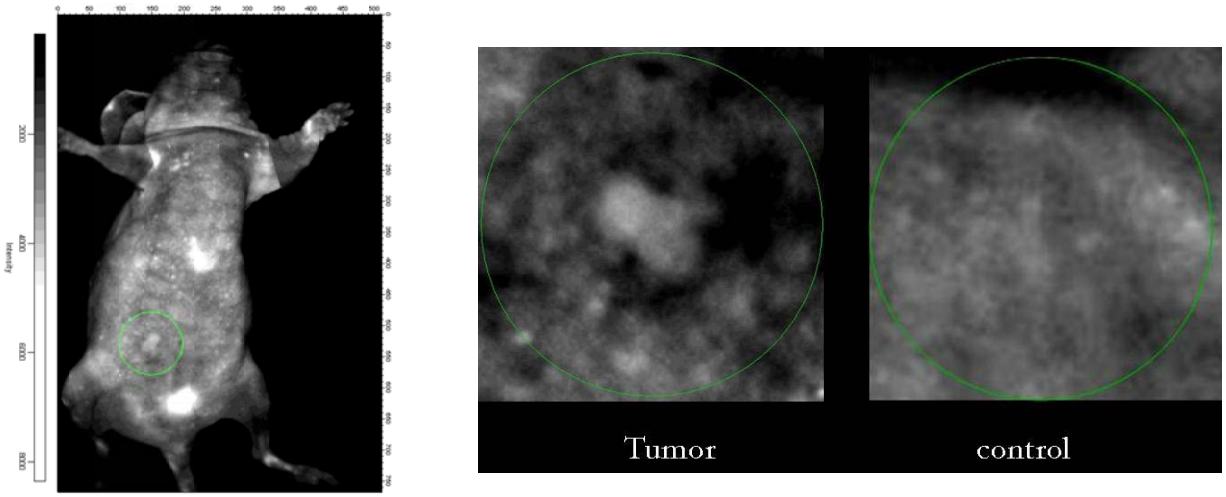

Images in fluorescence of a tumor-bearing mouse and higher magnification view of perfusion of tumor compared to contralateral mammary.

SPECT IMAGING AGENTS

Returning to SPECT, we have participated with our colleagues in evaluating a new imaging agent, Clioquinol. This agent targets areas with high transition metal concentrations. While it was originally developed to image plaque in Alzheimer's disease it is also effective in breast cancer. Thus we show below that the agent stains quite effectively a lymph node metastasis of breast cancer

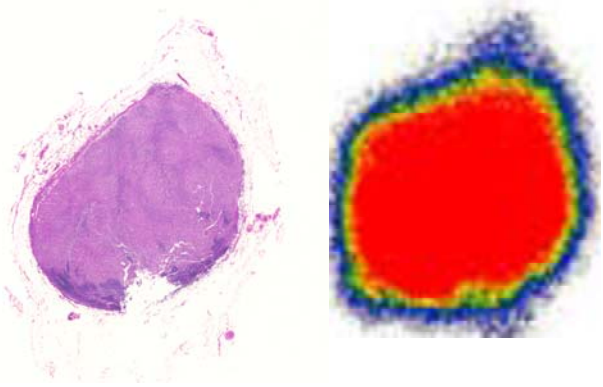

The figure shows the radioactivity distribution of ^{125}I-CQ in a tissue slice of lymph node together with a standard tumor stain in an adjacent slice. Intense uptake is shown in red, less intense in blue.

We also injected CQ into nude mice and obtained screen images without collimation

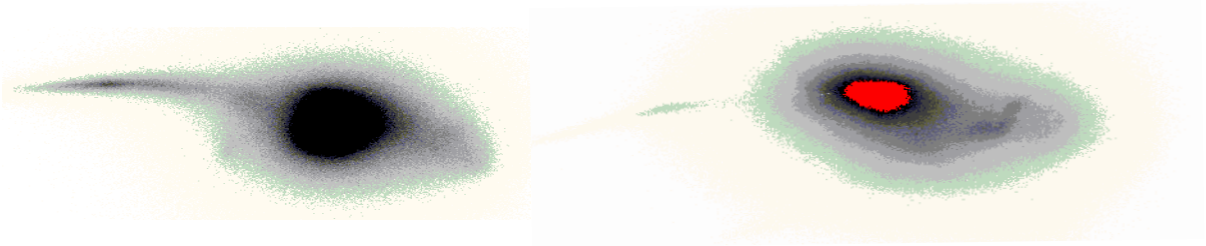

Storage phosphor screen images of BALB/c nude mice injected with ^{125}I-CQ: tumor-bearing mouse at right (MDA-435 Human BrCa) vs control at left. The control mouse shows a diffuse distribution but the tumor-bearing mouse shows accumulation in the flank.

KEY RESEARCH ACCOMPLISHMENTS

1) Completion of software for Light Emission Tomography (LET). Our reconstruction approach consists of two steps: light surface reconstruction to determine the geometry of turbid media boundaries and then source reconstruction inside the tissue by using a deblurring EM algorithm based on the diffusion equations. The method accounts for scattering.
2) Device: most tests are accomplished using a four-camera device. We have improved the noise performance of our CCD cameras with better cooling and with improved optics.
3) Techniques for the detection of metastases. We have used LET with the 4-headed device to detect metastases in the lung and head. We have demonstrated our ability to detect millimeter or sub-millimeter metastases in mice by light emission.
4) We have begun assessment of perfusion using fluorescence imaging. This is performed using the same device developed for LET.
5) we have continued development of a camera for micro-SPECT based on cooled, electron-multiplied Charge-Coupled Devices (EMCCDs) with which we are performing ongoing imaging experiments. We have developed software for image reconstruction with multiple pinholes.
6) We have also collaborated on the assessment of a new, promising SPECT imaging agent, clioquinol or Iodinated hydroxyquinoline.

REPORTABLE OUTCOMES

The methodology of Light Emission Tomography has been summarized in a recent publication: NV Slavine, MA Lewis, E Richer and PP Antich, Iterative reconstruction method for Light Emitting Sources based on the Diffusion Equation, Medical Physics 33 (61-68) 2006.

The application of LET to phantoms and to mice is reported in:
E Richer, NV Slavine, MA. Lewis, T Soesbe, S Seliounine, X Li, E Tsyganov, VD Kodibagkar, JW. Shay*, G.C. Gellert*, Z. G-D*, VJ. Bhagwandin*, RP. Mason, PP. Antich Light Emission Tomography: Visualizing Small Animal Biology in three dimensions. Prepared for submission, preprint enclosed.

Progress in multi-pinhole SPECT system software has been presented at the Second Biannual Workshop on Small-Animal SPECT imaging in Tucson, Arizona by NV Slavine (power point presentation).

Progress in Scatter Correction for Low-Energy Small Animal SPECT using Optical Surface Topography in a Dual Modality Imaging System has been presented at the Second Biannual Workshop on Small-Animal SPECT imaging in Tucson, Arizona by MA Lewis (power point presentation).

CONCLUSION

In conclusion, while the integration of the two modalities needs to be perfected to achieve maximum imaging usefulness, we have made progress towards establishing an imaging method and agents capable of translation to the clinic.

APPENDICES

1. NV Slavine, MA Lewis, E Richer and PP Antich, Iterative reconstruction method for Light Emitting Sources based on the Diffusion Equation, Medical Physics 33 (61-68) 2006

2. E Richer, NV Slavine, MA. Lewis, T Soesbe, S Seliounine, X Li, E Tsyganov, VD Kodibagkar, JW. Shay*, G.C. Gellert*, Z. G-D*, VJ. Bhagwandin*, RP. Mason, PP. Antich Light Emission Tomography: Visualizing Small Animal Biology in three dimensions. Submitted

Iterative reconstruction method for light emitting sources based on the diffusion equation

Nikolai V. Slavine,[a] Matthew A. Lewis,[b] Edmond Richer,[c] and Peter P. Antich[d]
Advanced Radiological Sciences, Department of Radiology, University of Texas Southwestern Medical Center, 5323 Harry Hines Boulevard, Dallas, Texas 75390-9058

(Received 14 June 2005; revised 13 October 2005; accepted for publication 17 October 2005; published 20 December 2005)

Bioluminescent imaging (BLI) of luciferase-expressing cells in live small animals is a powerful technique for investigating tumor growth, metastasis, and specific biological molecular events. Three-dimensional imaging would greatly enhance applications in biomedicine since light emitting cell populations could be unambiguously associated with specific organs or tissues. Any imaging approach must account for the main optical properties of biological tissue because light emission from a distribution of sources at depth is strongly attenuated due to optical absorption and scattering in tissue. Our image reconstruction method for interior sources is based on the deblurring expectation maximization method and takes into account both of these effects. To determine the boundary of the object we use the standard iterative algorithm—maximum likelihood reconstruction method with an external source of diffuse light. Depth-dependent corrections were included in the reconstruction procedure to obtain a quantitative measure of light intensity by using the diffusion equation for light transport in semi-infinite turbid media with extrapolated boundary conditions. © *2006 American Association of Physicists in Medicine*. [DOI: 10.1118/1.2138007]

Key words: bioluminescence imaging, diffusion equation, boundary condition, deblurring EM method, 3D-reconstruction

I. INTRODUCTION

A. Overview

Small animal imaging using bioluminescence sources (as with the Renilla or firefly luciferase reporter systems) has attracted much attention in recent years.[1–4] Cells transfected with light emitting probes can also be used to detect gene expression *in vivo*.[5–7] *In vivo* imaging of bioluminescence sources in animals offers a unique opportunity for noninvasive studies of cellular or molecular events to better understand the effects of human disease in animal models.[8,9] For efficient detection of bioluminescent probes in living animals, it is necessary to use high sensitivity low-noise detectors, such as cooled charged-coupled devices (CCDs) while advanced algorithms may be needed for image reconstruction. Several techniques have been developed in order to determine the location of an object in strongly scattering media using visible or near-infrared light.[10–13]

The solution uniqueness for bioluminescent imaging (BLI) reconstruction can be strengthened by incorporation of *a priori* information on the animal anatomy and optical properties.[14–17] This is a significant problem for any BLI reconstruction algorithm, and effective algorithms for distributed BLI sources are still an active area of research.

B. Reconstruction methods

Reconstruction algorithms must take into account the main optical properties of biological tissue: light absorption, scattering, and reflection at major interfaces. In this case, a model describing light transport in turbid media is critical for any reconstruction technique.[18] Widely used methods are the diffusion approach and Monte Carlo (MC) simulations,[19,20] both based on the radiative transfer equation (RTE).[10,14,21–23] The RTE is a Boltzmann-type nonlinear transport equation for the photon intensity. This equation is often impossible to solve analytically, and is usually simplified by a diffusion approximation[14,21] that describes the diffuse part of the radiative intensity. A disadvantage of this approach is the inaccuracy in predicting the light distribution near light sources and boundaries. The MC simulation, based on the RTE, is a computational method, which models the individual photon interactions in turbid media. This method is an accurate and powerful way to study photon transport in tissue requiring no simplifications, but needing extensive computational resources. This diffusion approach has been shown to be in good agreement with MC simulations and experiments.[1,19,24,25]

Three-dimensional- (3D-) source reconstruction is the primary goal of light emission tomography (LET), and this problem is formulated as an inverse problem based on the diffusion approximation.[14,26–28] Good results for 3D-optical reconstruction have also been obtained by using the finite element method (FEM).[29–32] We have recently completed preliminary tests of a bioluminescent LET system with multiple rotating, high sensitivity CCD cameras[33,34] to obtain 3D reconstructed images. Tests with different phantoms verify the utility of the approach and the accuracy of the 3D-source reconstruction algorithm.

In Ref. 31 two sources with $\sim$10 mm separation were reconstructed using a FEM algorithm. We present reconstruction results for two sources with the same separation using our new algorithm. The problem we are addressing

here is that of relating image to source intensity. For this purpose, using the diffusion approximation and balancing the internal and external intensities on the boundary of the media, we determine an initial order approximation for the photon fluence, and subsequently apply the iterative deblurring EM method[35,36] to obtain a final reconstruction result.

C. Light diffusion in tissue

To estimate the position and intensity of bioluminescence source one can describe photon propagation through tissue by the diffusion approximation:

$$\frac{1}{c_n}\frac{\partial\varphi(r,t)}{\partial t} = -D\nabla^2\varphi(r,t) - \mu_a\varphi(r,t) + S(r,t), \tag{1}$$

where $\varphi(r,t)$ is the isotropic fluence rate, D and μ_a are the diffusion and absorption coefficients, respectively, $S(r,t)$ is the internal light source distribution, and $r(x,y,z)$ is the distance away from the source in time t. For steady-state diffusion, according to the dipole source model[24,25] with extrapolated boundary, the photon fluence rate at the physical boundary can be expressed as a sum of contributions from the positive internal source $\varphi(r_s)$ and its negative image source above the tissue $\varphi(r_i)$:

$$\varphi(r) = \varphi(r_s) - \varphi(r_i) = S_0 e^{-\mu_{\text{eff}} r_s}\frac{(4\pi D)^{-1}}{r_s} - S_0 e^{-\mu_{\text{eff}} r_i}\frac{(4\pi D)^{-1}}{r_i}, \tag{2}$$

where $r_s=(z_s^2+r^2)^{1/2}$ and $r_i=(z_i^2+r^2)^{1/2}$ is the distance from the source and its image to point on the boundary, $\mu_{\text{eff}}=(\mu_a/D)^{1/2}$ is an effective attenuation coefficient. The surface radiance on the physical boundary is

$$L(r) = \frac{1}{4\pi}\varphi(r) + \frac{3}{4\pi}[\varphi(r_s)\Delta_s + \varphi(r_i)\Delta_i],$$

$$\Delta_\alpha = \frac{z_\alpha}{r_\alpha^2}(1 + r_\alpha\mu_{\text{eff}})D \quad \text{for } \alpha = s,i. \tag{3}$$

The reflectance of photons at the tissue-air interface that will reduce the fluence rate out of the tissue:

$$R(r) = R(r_s) - R(r_i) = \varphi(r_i)\Lambda_s - \varphi(r_i)\Lambda_i,$$

$$\Lambda_\alpha = \frac{z_\alpha}{r_\alpha^2}(1 + r_\alpha\mu_{\text{eff}}) \quad \text{for } \alpha = s,i. \tag{4}$$

Solutions for spherical surface or solid sources for homogeneous medium were presented previously[37] and those authors consider this approach useful for good qualitative estimates of signal level and positions of light sources for BLI.

D. Phantoms and light sources

We fabricated the phantoms and light sources following procedures from published articles.[38–40] The heterogeneous mouse shaped phantom (with dimensions that approximate the size of a typical mouse) was fabricated from clear polymer resin with TiO_2 powder as scattering material ($\mu_s'=9\ \text{cm}^{-1}$) and Pro JeT 900 NP ink as absorption medium ($\mu_a=0.3\ \text{cm}^{-1}$).[40] In addition, formalin fixed mouse organs—heart, kidneys, and liver—were placed close to the anatomical position inside the mouse phantom. A 3 mm-diam spherical light source (peak emission about 580 nm) was placed between heart and liver. The cylindrical shaped phantom, 5 cm long and 3 cm diameter, has a circular aluminum base through which an 18 gauge hypodermic needle was inserted. There are five different radial positions for the needle ranging from the center to just below the surface, with step size of 2.54 mm. The light is emitted from the tapered end of the optical fiber 1 mm in size which was threaded through the needle;[41] the peak wavelength of the light source tuned at 580 nm matches that of the firefly luciferase[39] *in vivo* spectrum, which extends to 680 nm; the source is isotropic and reproducible within the phantom. Single and multiple light sources are possible. The phantom can be rotated through 2π degrees for imaging with a single CCD camera; the phantom material is a solidified mixture of distilled water, agarose (Sigma A0169), and Intralipid. By changing the concentration of Intralipid from 0.25% to 2% the value of μ_s' can be varied from 2.5 to 15 cm^{-1} without any significant change to the μ_a.[38] These reduced scattering coefficients match those of typical mouse tissues.

II. IMAGE RECONSTRUCTION METHOD

Our reconstruction approach consists of two main steps: 3D-surface reconstruction used to determine the geometry of boundary—used to infer the distances from source to each point of the boundary—followed by estimation of source position and intensity inside the tissue by using deblurring EM algorithm based on diffusion equations (2)–(4).

A. 3D-surface reconstruction

The surface reconstruction is based on the ML method.[42] In this algorithm a sequence of image estimates is generated for the kth iteration:[43]

$$n_j^{k+1} = \frac{n_j^k}{\sum_{i=1}^{I} a_{ij}}\sum_{i=1}^{I}\frac{m_i}{q_i^k}$$

where

$$q_i^k = \sum_{j=1}^{J} a_{ij} n_j^k, \tag{5}$$

where n_j^{k+1} and n_j^k are image intensity values in the new and current estimate for the voxel j (the interior of the body is subdivided into voxels). The measured data m_i for each angular position of CCD collected along lines i which connect a voxel on the object's surface to the CCD, gave values proportional to the light intensity detected by the pixel; q_i^k is the expected count in line i for the current estimate n^k, and a_{ij} is the probability that a light quantum emitted at voxel j will be detected in the line i. Figure 1 shows examples of ML surface reconstruction for the cylindrical phantom with two

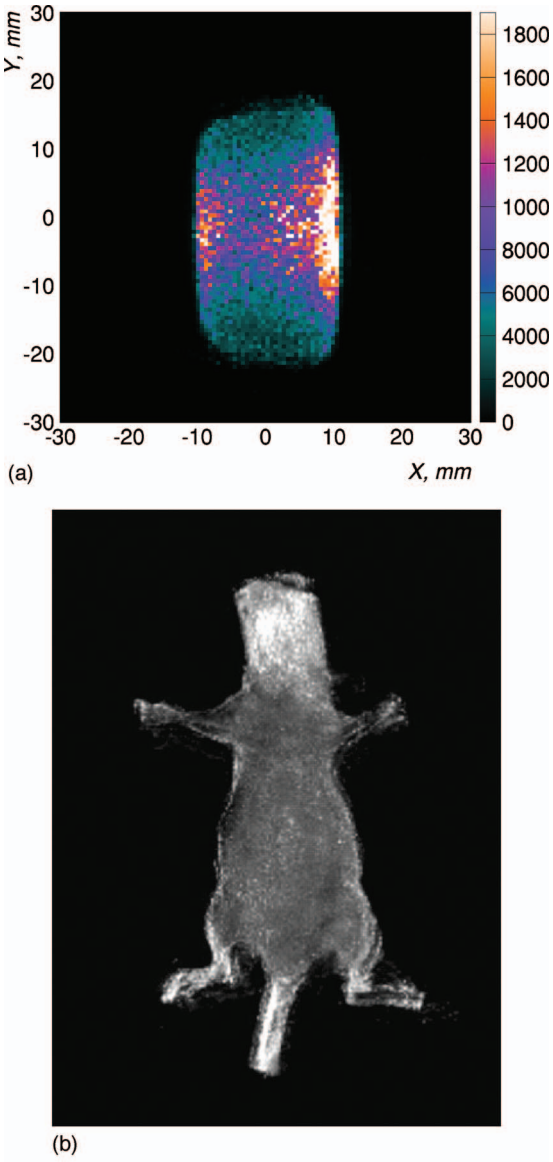

FIG. 1. 3D-surface reconstruction by ML method for phantom with two interior sources (a) and for living nude mouse from reflected light (b).

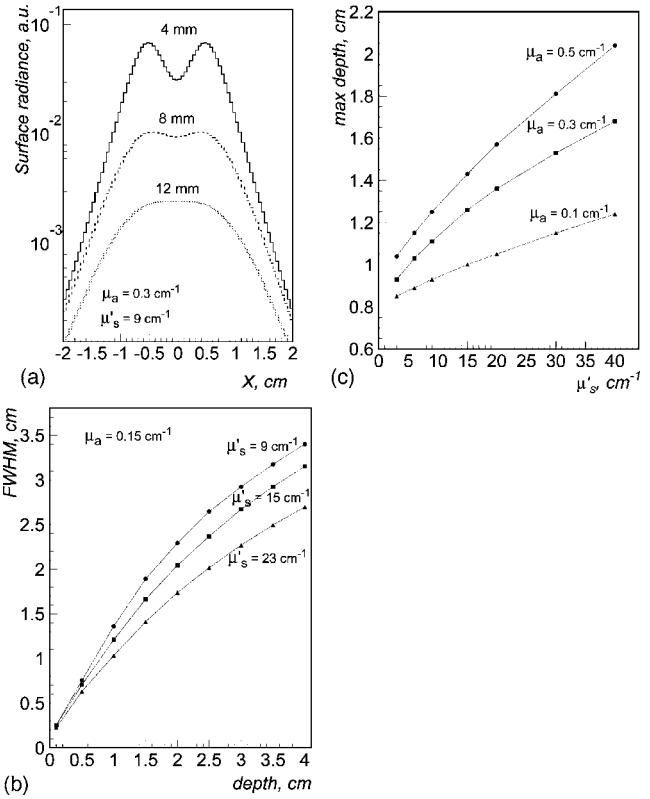

FIG. 2. Surface radiance peaks vs depth for two sources separated by 10 mm (a), FWHM as a function of source depth calculated for different reduced scattering coefficients (b), and maximum depth at which the two sources can be distinguished as separate peaks. The intensity curves are normalized to one at 1 mm depth.

interior light sources and for an externally illuminated living nude mouse. The second image demonstrates our ability to follow surfaces of varying curvature.

This approach permits not only a good estimation for irregular boundaries, but reconstructs location and intensity with a good resolution of any light sources emitted in air (in this case we can neglect correction for light diffusion). Note that in BLI experiments we in reality can use only a small part of the object surface due to limited light propagation in tissue. In this case we do not necessarily need to reconstruct the surface of the full mouse body or phantom. A more difficult problem is that of obtaining information about complex surface of heterogeneous objects (organs) inside the body or phantom.

B. 3D-source reconstruction inside the tissue

The diffusion approximation is very useful for estimating the surface photon intensity and light spot size depth-dependence for BLI experiments,[1,37] especially in the case of *in vivo* small animal studies.[1] Figure 2(a) shows surface radiance for two light sources separated by 10 mm embedded at different depths. Note that for these specific optical properties and source separation at the depth of 12 mm the two intensity peaks coalesce. The light spot size [Full width at half maximum (FWHM)] at the phantoms surface is shown in Fig. 2(b) as a function of depth for different values of μ_s' corresponding to different concentration of Intralipid. For the same value of the absorption coefficient, higher scattering coefficients give lower photon intensity levels but a better spatial resolution [see Eq. (3) and Ref. 1]. Figure 2(c) shows as a function of μ_s' and μ_a the maximum depth at which the two sources can be distinguished as separate peaks in the surface radiance. For typical optical properties of small animal tissues the maximum imaging depth is $\sim$1–1.5 cm. This depth is considered sufficient for imaging small animals such as mice and rats. Further advances are possible by examining the wavelength dependence of the emitted spectrum.

The reconstruction algorithm consists of the following steps.

Step 1. In order to estimate the source location we back-project our experimental data into the volume discretized

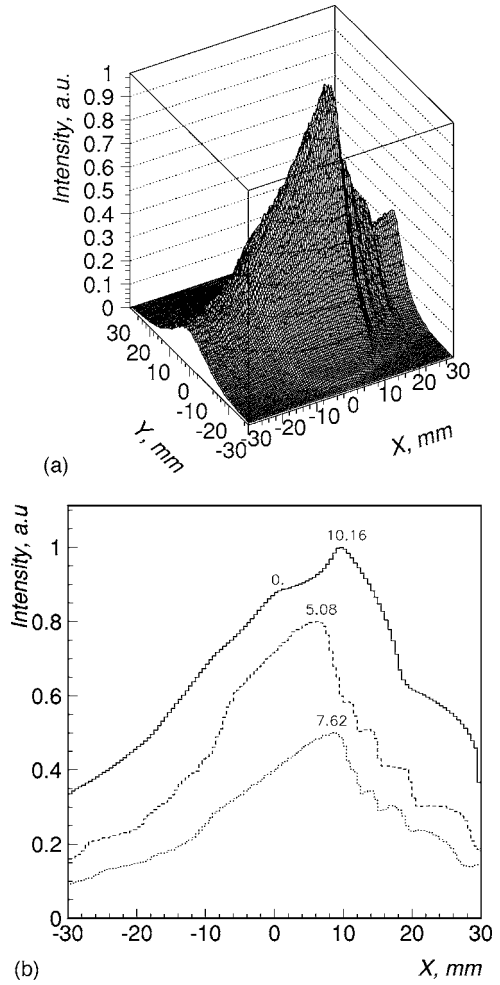

FIG. 3. 2D histogram showing maximum intensity for Intralipid phantom with a single source located at 7.62 mm from the center of system coordinate by X axis (a); slices of maximum intensities for phantoms with sources positioned at various X coordinates (b). Voxel size 0.5 mm.

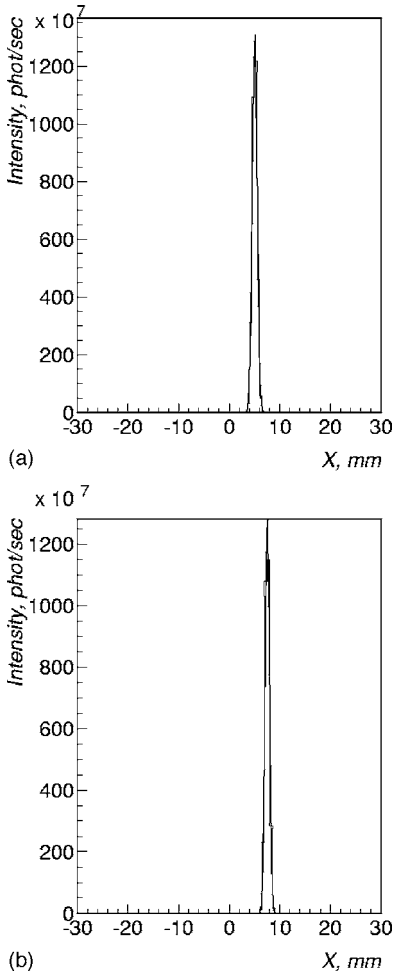

FIG. 4. 3D-reconstructed images of 1% Intralipid-filed medium phantoms displaced 5.08 mm (a), 7.62 mm (b) from the center of system coordinate by X axis.

into $N_x \times N_y \times N_z$ voxels. Two-dimensional (2D) histograms are then generated for each of the N_z depth planes and the X, Y position of relevant intensity peaks is determined [Fig. 3(a)]. Combining the results from all depth planes we obtain estimations for X, Y, and Z coordinates of all light sources in the reconstructed volume [Fig. 3(b)]. If the position of the light source exceeds the maximum detectable depth for *all imaging directions* [Fig. 2(a) for 12 mm depth], we need to use a more sophisticated method to obtain source coordinates estimates (FEM, MC, or Ref. 50), or use *a priori* information obtained from another imaging system (for example, CT, MRI, or OPET[44]) to estimate the heterogeneous optical properties of the intervening tissues.

Step 2. After estimation of source position we can take into account reflection on boundary[45–47] (4), calculate intensity values for each voxel j, and subtract this reflection contribution. We obtain the transmitted part of intensity from the CCD data. The diffusion equation is used to determine the balance intensities for internal sources N_s for the surface element in a single voxel.

Step 3. Next for each voxel j we can determine a "zeroth" order approximation φ_j^0 (i.e., initial guess as an input image, which contains all diffuse light information) using the solution for photon fluence:

$$\varphi_j^0 = (\rho \otimes \varphi + \hat{n})_j \cong \frac{1}{\sum_{i=1}^{I} x_{ij} p_i^t} \sum_{i=1}^{I} x_{ij} p_i^0 \sum_{s=1}^{s=N_s} S_o' \times \exp(-\mu_{\text{eff}} r_{js})/r_{js}, \quad (6)$$

where ρ is a point-spread function, φ is a real value of photon fluence, $\hat{n}$ is a noise term, and x_{ij} is the path length of line i through voxel j, p_i^t and p_i^0 are intensities in CCDs from source in media and in air. Here we have utilized the basis function from the semi-infinite geometry as a first approximation to the diffuse photon propagator.

Step 4. After correcting all voxels we apply the deblurring EM algorithm[36] for final 3D-image reconstruction by using approximation (6)

TABLE I. Source positions and FWHM for *X*, *Y*, and *Z* profiles for the air and Intralipid phantoms reconstruction.

	Air				Intralipid			
		FWHM				FWHM		
X position in phantom, (mm)	*X* position	*X*	*Y*	*Z*	*X* position	*X*	*Y*	*Z*
Single source phantoms								
0.0	−0.08	0.89	0.91	0.90	0.098	1.15	1.18	1.16
2.54	2.58	0.91	0.93	0.92	2.64	1.18	1.21	1.20
5.08	5.03	0.86	0.89	0.88	5.06	1.19	1.22	1.20
7.62	7.60	0.89	0.92	0.91	7.52	1.04	1.09	1.08
10.16	10.01	0.91	0.93	0.92	9.98	1.20	1.24	1.19
Dual source phantom								
0.0	0.07	1.05	1.09	1.06	−0.25	1.32	1.38	1.33
10.16	10.03	1.05	1.08	1.08	10.27	1.17	1.22	1.18

$$\varphi_j^{n+1} = \varphi_j^n \left\{ \hat{\rho} \otimes \left(\frac{\varphi_j^0}{\rho \otimes \varphi_j^n} \right) \right\}, \tag{7}$$

where $\otimes$ denotes convolution procedure based on the discrete fast Fourier transform (FFT).[48] Parameters ρ and $\hat{\rho}$ are the deblurring kernels (for example, Gaussian functions) and can be changed with number of iterations n.

III. RESULTS

In our imaging system multiple high sensitivity CCD cameras simultaneously record views from different angles and a computer controlled rotation mechanism allows imaging at intermediate angular positions, as required for surface and interior sources 3D reconstructions. The CCDs data for each of the twenty (18° angle step) positions were combined for all rotation angles and used for reconstruction procedure.

A. Single source phantom

The field of view of $60 \times 60 \times 60$ mm was subdivided into voxels of 0.5 mm^3 in size. The deblurring kernel parameters ρ and $\hat{\rho}$ were equal and started at 6 mm (first few iterations) and reduced to 1.2 mm during the 310 iterations. Figure 4 shows the example of *X* profiles (*Y* and *Z* positions of sources were in the center of system coordinate) for the deblurring EM reconstructed sources at 5.08 and 7.62 mm [compare with Fig. 3(b)]. Each profile is fitted with a Gaussian function, and the FWHM of the distribution is taken as the reconstructed source size (see Table I for results for all source positions).

It can be seen that the reconstructed source sizes are in excellent agreement with the actual size. The total light intensity in air (not shown here) and Intralipid differed by less then 5%. For example, for phantom with source displaced by 10.16 mm in air the emitted light intensity was 1.44×10^{10} photon/s vs 1.37×10^{10} photons/s in Intralipid.

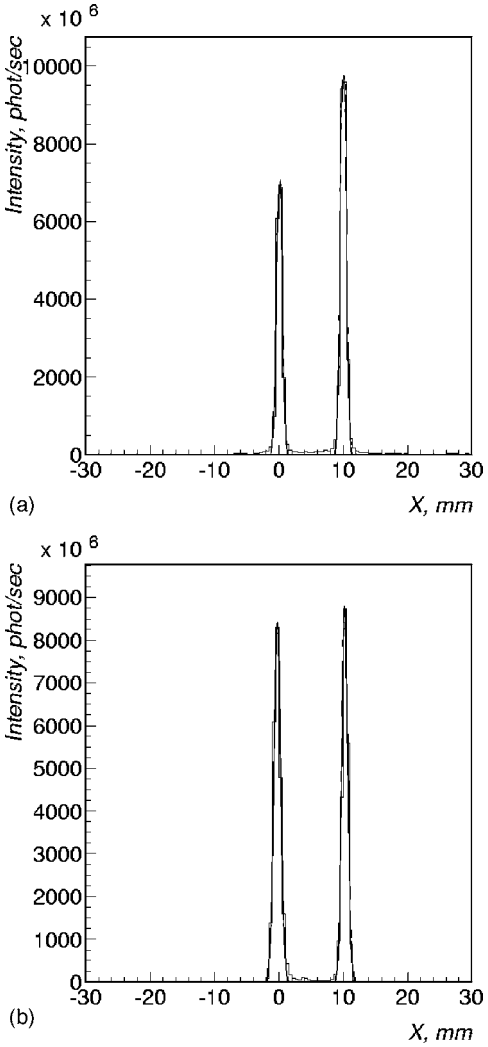

FIG. 5. 3D reconstruction for dual source phantom with separation 10.16 mm: (a) in air and (b) in 1% Intralipid phantom.

B. Dual source phantom

The field of view for this phantom was same as for single sources: $60 \times 60 \times 60$ mm with voxel size 0.5 mm^3. The deblurring kernel parameters ρ and $\hat{\rho}$ were equal and varied from 9 mm (few first iterations) to 1.2 mm during the 150 iterations. Figure 5 shows the *X* profiles for the EM deblurring reconstructed dual point source with 10.16 mm separations in air and in Intralipid [compare with Fig. 3(b)]. The values of FWHM obtained from the Gaussian fit are taken as reconstructed source sizes and are in a good agreement with physical dimensions (see Table I). The two optical sources in air were not identical.

The total light intensity in air and Intralipid differed by less than 8%—intensity in air 9.6×10^9 photon/s vs 8.8×10^9 photons/s in Intralipid.

C. Volume size quantification

Quantifying the tumor size is important in cancer research[4,49] as it permits an estimate of cell numbers. PC3-

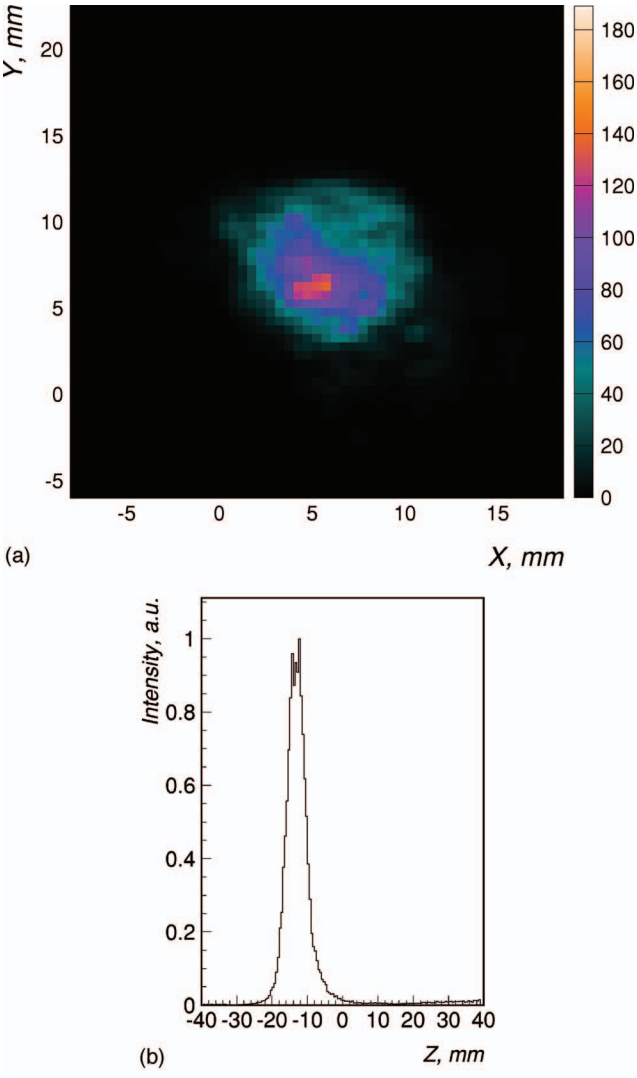

FIG. 6. *XY* and *Z* profiles for BLI tumor size experiments after 5 ML iterations.

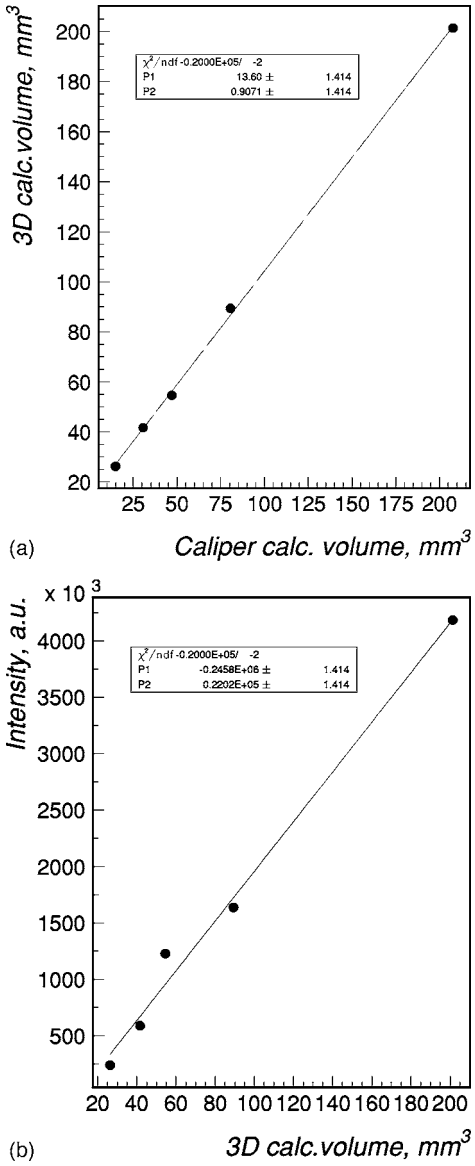

FIG. 7. Correlation of the caliper measurements of tumor size (a) and peak of Intensity (b) with 3D-volume reconstruction.

LUC cells injected in the flank of live nude mice were imaged in the LET system[33] using 5 s exposure time from 20 angular directions for each measurement.

Tumor sizes were determined after reconstruction by ML algorithm (see the example in Fig. 6) using 0.5 mm cubic voxels and five iterations for each calculation. The values of FWHM for *X*, *Y*, and *Z* directions obtained from the Gaussian fit were used to determine tumor sizes. Figure 7(a) shows a good agreement with the caliper measurements in the same tumors and is very close to the line with zero intercept and a slope of 1.

The correlation between the peak intensity of light emitted by a tumor and its volume obtained from ML reconstruction is plotted in Fig. 7(b). Because we used the same conditions for all tumor measurements and same parameters for surface reconstruction we expect that tumor intensity will be correctly indicative of tumor volume.

D. Mouse shaped phantom

In order to demonstrate the source reconstruction in the context of both a complex surface geometry and heterogeneous media we used a phantom that approximates the shape and dimensions of a typical mouse. A superposition of images (source and shape) in Fig. 8 shows that both position and source size were correctly determined by the 3D algorithm. The number of iterations for surface reconstruction was 5, and 100 for source reconstruction. Position of the center after reconstruction $X=1.67$ mm, $Y=5.76$ mm, and $Z=0.51$ mm while FWHM was 3.45, 3.64, and 3.52 mm, respectively.

Here we demonstrate source position reconstruction only: we took into account solution for spherical source[37] and light intensity correction for different optical properties of mouse organs at known location and sizes (*a priori* information). In the reconstruction of *in vivo* experiments, the complex calculations for determining intensities and positions would be greatly facilitated by the necessary information about mouse

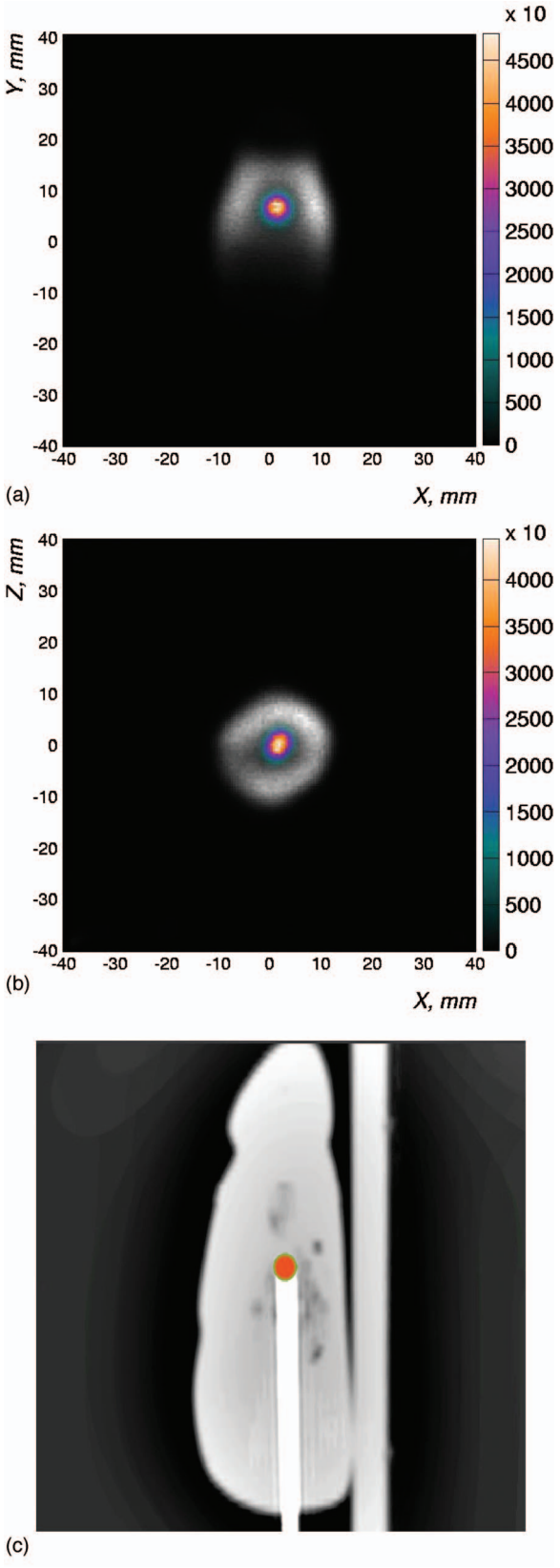

FIG. 8. Coronal (a) and transaxial (b) images of mouse shaped heterogeneous phantom. The center of source was located in position $X=2$ mm, $Y=5$ mm, and $Z=0$ mm. Voxel size=0.5 mm. Black and white image represents boundary of surface estimates and color portion represents image after EM deblurring. (c) Co-registered CT (imaged with GE CT/I, 3D rendering using VolView 2.0, Kitware, Inc), and reconstructed light source.

anatomy and the corresponding heterogeneous optical properties.

IV. CONCLUSIONS

Our phantom and BLI experiments have provided quantitative data showing the tomographic capabilities of the imaging system[33,34] and reconstruction algorithms for appropriate depths. The reconstruction approach is applicable to complex geometries, can be used with any suitable photon propagation model, and is amenable to fast imaging calculations (depending on number of voxels, iterations and amount of experimental data from CCDs). The number of iterations (image updates) in source reconstruction procedure was chosen to get a good agreement between source size resolution and light intensity. The average processing time per image update for ML reconstruction was about 350 ms (Pentium 4) and for deblurring EM procedure was a few seconds (time dependent upon FFT algorithm).

The imaging procedure and reconstruction software were verified using single and dual source phantoms. The source dimensions and separation are in a good agreement with expected values. We find some degree of competition between the source sizes and intensity because optimizing the reconstruction parameters for source intensity may have counter effects on source size. Solution of this problem is based on comparing the spectrum measured in the imaging experiment with that emitted by sources in air and will be outlined in future work.

Image reconstruction can be difficult or even impossible (for heterogeneous media especially) if information is missing due to incomplete data acquisition or sources with limited photon propagation. Our group plans to overcome excessive attenuation with improved technology. However it may be possible to use neural network method with input-dependent weights[50] combined with EM algorithm for missing data[51] or Monte Carlo methods to get useful tool for BLI reconstruction. We are actively investigating alternative algorithms for solving the main problem of BLI—how to reconstruct real distributed sources inside living mouse tissue with high resolution. Information from different small animal imaging modalities[5,44,52] may be useful in providing the additional *a priori* anatomic information.

In conclusion, this study provides further evidence validating the use of bioluminescence to investigate tumor growth (see Fig. 7),[34,49] especially for small tumors or tumors that are less readily accessible to measurement by calipers.[4]

ACKNOWLEDGMENTS

We are grateful to Dr. R. Mason, Dr. R. McColl, Dr. R. Parkey, Dr. V. Kadibagkar, and Dr. E. Tsyganov for their advice and collaboration and our students T. Soesbe and Xiufeng Li for valuable help with BLI and phantom experiments.

[a]nikolai.slavine@UTSouthwestern.edu
[b]matthew.lewis@UTSouthwestern.edu
[c]edmond.richer@UTSouthwestern.edu

[d]peter.antich@UTSouthwestern.edu

[1]B. W. Rice, M. D. Cable, and M. B. Nelson, "In vivo imaging of light-emitting probes," J. Biomed. Opt. **6**, 432–440 (2001).
[2]C. H. Contag and M. N. Bachmann, "Advances in bioluminescence imaging of gene expression," Annu. Rev. Biomed. Eng. **4**, 235–260 (2002).
[3]T. F. Massound and S. S. Gambhir, "Molecular imaging in living subjects: Seeing fundamental biological processes in a new light," Genes Dev. **17**, 545–580 (2003).
[4]Z. Paroo, R. A. Bollinger, D. A. Braasch, E. Richer, D. R. Corey, P. P. Antich, and R. P. Mason, "Validating bioluminescence imaging as a high-throughput, quantitative modality for assessing tumor burden," Molecular Imaging **3**, 1–8 (2004).
[5]R. Blasberg, "In vivo molecular-genetic imaging: Multi-modality nuclear and optical combinations," Nucl. Med. Biol. **30**, 879–888 (2003).
[6]S. R. Cherry, "In vivo molecular and genomic imaging: New challenges for imaging physics," Phys. Med. Biol. **49**, R13–R48 (2004).
[7]V. Ntziachristos, J. Ripoll, L. Wang, and R. Weissleder, "Looking and Listening to light: The evolution of whole-body photonic imaging," Nat. Biotechnol. **23**, 313–320 (2005).
[8]H. R. Herschman, "Molecular imaging: Looking at problems, seeing solutions," Science **302**, 605–608 (2003).
[9]J. Marx, "Building better mouse models for studying cancer," Science **299**, 1972–1975 (2003).
[10]A. D. Klose and A. H. Hielsscher, "Fluorescence tomography with simulated data based on the equation of radiative transfer," Opt. Lett. **28**, 1019–1021 (2003).
[11]V. Ntziachristos, C. Tung, C. Bremer, and R. Weissleder, "Fluorescence molecular tomography resolves protease activity in vivo," Nat. Med. **8**, 757–760 (2002).
[12]A. H. Hielscher, "Model-based iterative image reconstruction for photon migration tomography," Proc. SPIE **3**, 106–117 (1997).
[13]H. Dehghani, B. A. Brooksby, B. W. Pogue, and K. D. Paulsen, "Effects of refractive index on near-infrared tomography of the breast," Appl. Opt. **44**, 1870–1878 (2005).
[14]G. Wang, Y. Li, and M. Jiang, "Uniqueness theorems in bioluminescence tomography," Med. Phys. **31**, 2289–2299 (2004).
[15]G. Wang, E. A. Hoffman, G. McLennan, L. Wang, M. Suter, and J. Meinel, "Development of the first bioluminescent CT scanner," Radiology **229**, 566 (2003).
[16]W. Cong, D. Kumar, Y. Liu, A. Cong, and G. Wang, "A practical method to determine the light source distribution in bioluminescent imaging," Proc. SPIE **5535**, 679–686 (2004).
[17]M. Schweiger and S. R. Arridge, "Optical tomographic reconstruction in a complex head model using a priori region boundary information," Phys. Med. Biol. **44**, 2703–2721 (1999).
[18]S. R. Arridge and J. C. Hebden, "Optical imaging in medicine. II. Modeling and reconstruction," Phys. Med. Biol. **42**, 841–853 (1997).
[19]S. T. Flock, M. S. Patterson, B. C. Wilson, and D. R. Wyman, "Monte Carlo modeling of light propagation in highly scattering tissues. I. Model predictions and comparison with diffusion theory," IEEE Trans. Biol. Eng. **36**, 1162–1168 (1989).
[20]L. Wang, S. L. Jacques, and L. Zheng, "MCML—Monte Carlo modeling of light transport in multi-layered tissues," Comput. Methods Programs Biomed. **47**, 131–146 (1995).
[21]A. Ishimaru, *Wave Propagation and Scattering in Random Media* (IEEE, Oxford, 1977).
[22]S. Shandrasekhar, *Radiative Transfer* (Dover, New York, 1960).
[23]V. Venugopalan and B. J. Tromberg, "Radiative transport in diffusion approximation: An extension for highly absorbing media and small source-detector separations," Phys. Rev. E **58**, 2395–2407 (1998).
[24]M. S. Patterson, B. Chance, and B. C. Wilson, "Time resolved reflection and tranmittance for the non-invasive measurement of tissue optical properties," Appl. Opt. **28**, 2331–2336 (1989).
[25]A. H. Hielscher, S. L. Jacquest, L. Wang, and F. K. Tittel, "The influence of boundary conditions on the accuracy of diffusion theory in time-resolved reflectance spectroscopy of biological tissue," Phys. Med. Biol. **40**, 1957–1975 (1995).
[26]T. J. Connolly and D. J. Wall, "On an inverse problem, with boundary measurements, for the steady state diffusion equation," Inverse Probl. **4**, 995–1012 (1988).
[27]S. R. Arridge, "Optical tomography in medical imaging," Inverse Probl. **15**, R41–R93 (1999).
[28]V. A. Merkel and J. C. Schotland, "Inverse scattering for the diffusion equation with general boundary conditions," Phys. Rev. E **64**, 035601(R) (2001).
[29]M. Schweiger, S. R. Arridge, M. Hiraoka, and D. T. Delpy, "The finite element method for the propagation of light in scattering media: Boundary and source conditions," Med. Phys. **22**, 1779–1792 (1995).
[30]S. R. Arridge, M. Dehghani, M. Schweiger, and E. Okada, "The finite element method for the propagation of light in scattering media: A direct method for domains with nonscatering regions," Med. Phys. **27**, 252–264 (2000).
[31]X. Gu, Q. Zhang, L. Larcom, and H. Jiang, "Three-dimensional bioluminescence tomography with model-based reconstruction," Opt. Express **12**, 3996–4000 (2004).
[32]M. A. Lewis, N. Slavine, E. Richer, and P. Antich, "On the minimally-resolvable separation of few point sources in turbid media," Opt. Lett. (submitted).
[33]E. Richer, N. Slavine, M. Lewis, G. Gellert, Z. Dikmen, V. Bhagwandin, J. Shay, R. P. Mason, and P. Antich, "Three dimensional light emission tomography using multiple rotating CCD cameras," The Third Annual Meeting of the Society for Molecular Imaging, St. Louis, MO, 2004, p. 216, submitted to Nature Methods.
[34]Z. G. Dikmen, G. Gellert, P. Dogan, R. Mason, P. Antich, E. Richer, W. E. Wright, and J. W. Shay, "A new diagnostic system in cancer research: Bioluminescent imaging," Turk. J. Med. Sci. **35**, 65–70 (2005).
[35]Y. L. You and M. Kaveh, "A regularization approach to join blur identification and image restoration," IEEE Trans. Image Process. **5**, 416–427 (1996).
[36]M. Jiang, G. Wang, M. W. Skinner, and J. T. Rubinstein, "Blind deblurring of spiral CT images," IEEE Trans. Med. Imaging **22**, 837–845 (2003).
[37]W. Cong, L. V. Wang, and Ge Wang, "Formulation of photon diffusion from spherical bioluminescent sources in an infinite homogeneous medium," BioMed. Eng. OnLine **3**, 1–6 (2004), http://www.biomedical-engeneering-online.com
[38]R. Cubeddu, A. Pifferi, P. Taroni, A. Torricelli, and G. Valentini, "A solid tissue phantom for photon migration studies," Phys. Med. Biol. **42**, 1971–1979 (1997).
[39]R. L. Larossa, *Bioluminescence Methods and Protocols* (Methods in Molecular Biology) (Humana, 1998).
[40]M. Firbank and D. T. Delpy, "An improved design for a stable and reproducible phantom material for use in near-infrared spectroscopy and imaging," Phys. Med. Biol. **40**, 955–961 (1995).
[41]T. C. Soesbe, N. V. Slavine, E. Richer, and P. P. Antich, "A solid tissue phantom for tomographic bioluminescence imaging studies," Radiology Department of the University of Texas Medical Center, Dallas, 17 December (2004), pp. 1–13 (unpublished).
[42]R. T. Whitaker and J. Gregor, "A maximum likelihood surface estimator for dense range data," IEEE Trans. Pattern Anal. Mach. Intell. **24**, 1372–1387 (2002).
[43]L. A. Shepp and V. Vardi, "Maximum likelihood reconstruction for emission tomography," IEEE Trans. Med. Imaging **1**, 113–122 (1982).
[44]D. L. Prout, R. W. Silverman, and A. Chatziioannou, "Detector Concept for OPET—A combined PET and optical imaging system," IEEE Trans. Nucl. Sci. **51**, 752–756 (2004).
[45]A. Kienle and M. S. Patterson, "Improved solutions of the steady-state and the time-resolved diffusion equations for reflectance from semi-infinite turbid medium," J. Opt. Soc. Am. A **14**, 246–254 (1997).
[46]W. Lihong, "Rapid modeling of diffusion reflectance of light in turbid media," J. Opt. Soc. Am. A **15**, 936–944 (1998).
[47]G. W. Faris, "Diffusion equation boundary conditions for the interface between turbid media: comment," J. Opt. Soc. Am. A **19**, 519–520 (2002).
[48]C. S. Burrus and T. W. Parks, *Discrete Fourier Transform, Fast Fourier Transform and Convolution Algorithms* (Wiley, New York, 1984).
[49]S. H. Thorne and C. H. Contag, "Using in vivo bioluminescence imaging to shed light on cancer biology," Proc. IEEE **93**, 750–762 (2005).
[50]Neural Networks, EE048941, "EM Algorithms," Technion, 2001.
[51]G. J. McLachlan and T. Krishnan, *The EM Algorithm and Extensions* (Wiley, New York, 1997).
[52]J. M. Park and S. S. Gambhir, "Multimodality radionuclide, fluorescence, and boluminescence small animal imaging," Proc. IEEE **93**, 771–783 (2005).

Light Emission Tomography (LET):

Visualizing Small Animal Biology

in Three-Dimensions.

Edmond Richer, Nikolai Slavine, Matthew A. Lewis, Todd Soesbe, Serguei Seliounine, Xiufeng Li, Edward Tsyganov, Vikram D. Kodibagkar, Jerry W. Shay*, Ginelle C. Gellert*, Z. Gunnur Dikmen*, Vikash J. Bhagwandin*, Ralph P. Mason, Peter P. Antich

Departments of Radiology and *Cell Biology,

University of Texas Southwestern Medical Center, Dallas, TX

Running title: **Light Emission Tomography**

Keywords: optical tomography, bioluminescence, luciferase, gene reporter, tumor

Peter P. Antich, Ph.D., D.Sc.,

Department of Radiology,

UT Southwestern Medical Center at Dallas,

5323 Harry Hines Blvd.,

Dallas, TX 75390-9058

Tel: (214) 648-2856

Fax: (214) 648-2991

E-mail: Peter.Antich@UTSouthwestern.edu

Abstract

Bioluminescent imaging of cells expressing luciferase is a valuable noninvasive technique for investigating molecular events and tumor growth in the living animal. Current usage is often confined to planar imaging, but a volumetric imaging approach would obviously enhance the applicability to biomedicine, for instance by attributing the signal to a specific organ or tissue. What is needed is a rapid, automated method to obtain and visualize volumetric images. We report here a novel approach using multiple rotating CCD cameras, and image reconstruction software to provide the desired representation of light emitting cells within living mice. Validation experiments were performed in simple and complex phantoms, and several *in vivo* examples are presented. Volumetric images were obtained in an experimental lung metastasis xenograft model with A549-LUC human tumor cells growing in the lungs of a nude mouse. In a second model of lung metastasis MDA-MB-231-LUC breast tumor cells were also imaged by MRI, confirming the location of the tumors detected by LET. Volumetric LET imaging proved to be superior to planar BLI in assessing the tumor volume in the case of PC3-LUC human prostate cancer cells growing in the flank of nude mice.

INTRODUCTION

The ability of bioluminescent imaging (BLI) to assess gene expression in living animals promises new insight into developmental biology and gene therapy related to many diseases[1-3]. Recent reports investigate conditions ranging from cardiovascular development to tumor growth and the assessment of diverse promoter elements[4-9]. The technique is primarily based on the luciferase gene (obtained from the North American firefly, *Photinus pyralis*), which is readily introduced into diverse cells and expressed effectively. When the substrate, D-luciferin, is administered to such cells or to an animal host, a bioluminescent reaction occurs emitting light that can be detected using a cooled charged-couple device (CCD) digital camera.

To date, BLI is widely used as a planar technique, although its effectiveness is limited for visualization (localization of cell population) and quantitation (tumor size estimation)[10]. The limits are due to the fact that the intensity and distribution of the signal captured by the BLI camera at the animal's skin surface are strongly influenced by the intervening tissues resulting in an attenuated and diffused signal at the skin surface of the animal through both scattering and absorption[11, 12].

Indeed, tomography has been the goal of many research efforts, but it still remains to be demonstrated *in vivo*. Weissleder *et al*. have reported the design of an optical tomography system[13, 14], but their method was applied only to fluorescence imaging and requires light excitation sources. There has been a

report of images of bioluminescence *in vivo* from multiple directions using a rotating mirror system[15], and a commercial system is now available based on a single CCD camera. Gu *et al.* reported a three-dimensional bioluminescence tomography with a model based Finite Element Algorithm (FEM)[16]. Recently Chaudhari *at al.* showed hyperspectral and multispectral bioluminescent tomography [17], that requires imaging using six filters at different wavelengths. Computer simulations for a combined optical-PET system were also shown by Alexandrakis *et al* [18]. We reported an iterative method based on the diffusion equation to reconstruct light emitting sources in homogeneous phantoms[19].

The necessary next step is that of obtaining in vivo three-dimensional images and applying them to biological studies. We report here on our experience on *in vivo* 3D reconstruction of bioluminescence using light emission tomography (LET) to study metastasis.

RESULTS

Device and Technological Rationale

A significant problem for imaging a tumor or organ within an animal is that intervening tissues can totally or partially obscure the light emitted in the direction of a camera. The light emission may, however, be recovered from other viewing angles. Furthermore, bioluminescence is a dynamic process and light intensity varies significantly and rapidly after substrate administration [9], limiting the amount of time available for imaging. To overcome these problems it is

important to observe the animal from as many directions as possible simultaneously. We therefore designed and built an optical imaging system with multiple cameras that surround the subject in the transverse plane permitting the simultaneous acquisition of images from different angular directions. Currently, we employ four cameras and twenty orientations provided by a computerized system, which rotates the cameras around the longitudinal axis in 18 degree steps.

Figure 1 shows a schematic diagram of the system and eight representative images showing overlaid bioluminescent signal and external light images. The system uses innovative analysis and reconstruction software capable of providing full 3-D reconstruction and tomographic imaging.

Validation studies in phantoms verified the utility of the approach and accuracy of the 3D reconstruction algorithms. Before turning to *in vivo* imaging, we describe three phantoms of increasing complexity: a homogeneous diffusing cylinder and both homogeneous and heterogeneous mouse-shaped phantoms.

Homogeneous cylindrical phantom

Figure 2a shows the experimental setup with a 30 mm diameter cylindrical phantom filled with 1 % Intralipid / 1% agarose gel (Intralipid gel for brevity), which approximates light scattering in tissues. An optical fiber (1 mm diameter) was placed in the phantom before congealing the filling mixture and was optically coupled to a 560nm LED, a wavelength appropriate for simulating BLI emission.

A set of 20 images was obtained for each experiment by rotating the phantom 18° at a time.

The total amount of light captured at each imaging angle both in air and Intralipid phantom is presented in Figure 2b, obtained while keeping the light source intensity constant. The fiber optic source in air shows a small variation due to changes in distance from the lens. When the source was immersed in Intralipid gel it was noted that for angles between 0 and 180°, when the light source is closest to the camera, up to 4 times more light was captured than for the source in air, as the scattering of light in the phantom caused a significant increase in the photon flux toward the objective. When the source was in the position furthest from the camera (270°) only half as much light was captured, because the light source was shadowed by the body of the phantom. Overall, a variation of almost an order of magnitude was observed when imaging this phantom at different angles, showing the limited precision and reliability of a quantitative assessment from single planar images. This effect may be expected to affect animal studies, when light is emitted at depth within the body from multiple sources, such as small metastatic tumors in the lungs or other internal organs.

Figures 2c and 2d show images obtained first in air and then in Intralipid gel, with the fiber displaced 10 mm from the center at a viewing angle of 180°. A cross-section through the reconstructed 3D image is also shown for each case. The position of the source was correctly identified by the reconstruction

algorithm. The total light signal in air and Intralipid differed by only 3% (1,435 x 10^7 photons/sec for air vs. 1,390 x 10^7 photons/sec for Intralipid), further showing the quantitative nature of the 3D reconstruction algorithm. Confirmatory results were also obtained for multiple light sources, both in air and Intralipid, e.g., for two sources separated in depth by 10 mm (Fig. 2e).

Homogeneous mouse shaped phantom

In order to investigate the LET reconstruction in the context of a complex body surface, a mouse shaped 1% Intralipid gel phantom with a 9.5 mm diffuse spherical light source embedded in the thoracic region was imaged on the LET system. Figure 3a shows a longitudinal section of the phantom with the reconstructed source cross-section overlay. The reconstructed source is 10 mm in size, in good agreement with the physical dimensions, and at the correct location (within 1mm).

Heterogeneous mouse shaped phantom

To demonstrate the effectiveness of LET in the context of both a complex surface geometry and heterogeneous, diffusing and absorbing media, a mouse shaped phantom was fabricated from clear polymer resin with TiO_2 powder as scattering material and Pro Jet 900NP ink as absorbing medium. The optical properties of these materials approximate those of the animal tissue, with an absorption coefficient $\mu_a = 0.3$ cm^{-1} and the reduced scattering coefficient $\mu_s' = 9$ cm^{-1} at 610 nm [20]. In addition, formalin fixed mouse organs (heart, kidneys, and liver) were

placed in anatomical position, and a 3 mm spherical light source was placed between the heart and liver such that the emitted light passed through the organs before reaching the surface (Fig. 3b). After LET data acquisition and reconstruction, the phantom was imaged by CT and the two images were overlaid. As seen in Figure 3(c-f) both the position and the size of the source were correctly determined by the LET algorithm; LET and CT are in excellent agreement (error < 1mm).

***In vivo* imaging**

A549-LUC human lung tumor cells (10^6) were injected IV in a nude mouse (BALBc/nu/nu). After 63 days the lung-colonizing experimental metastases were imaged following D-luciferin injection (450 mg/kg, SQ) in the anesthetized mouse. A set of 20 images, 18º apart, was obtained using 1 min exposure starting 3 min post-injection of D-luciferin (Fig. 1). For each camera position, an externally illuminated image of the mouse was obtained for co-registration.

Data reconstruction provided a 3-D model of the lung tumors (Fig. 4a and Supplementary Movie S1). The algorithm was also applied to images obtained using light reflected from the skin under external illumination and the two data sets combined (Fig. 4b). Coronal cross-sections are presented in Figure 4c, emphasizing the information contained in the volumetric data. Intense local foci are apparent with a more diffuse background distribution outlining the anatomy of the lungs. Pathologic studies after sacrifice confirmed that the presence of A549-

LUC tumor cells dispersed throughout the lobes of the lungs with multiple metastatic foci. Staining of intact lungs by injection of India ink directly into the trachea indicates approximately 10^3 metastatic foci per mouse (Fig. 4d), as confirmed by sectioning of histological specimens (data not shown).

***In vivo* comparison with MRI**

Stably luciferase transfected MDA-MB-231-LUC human breast tumor cells (10^6) were injected IV in a nude mouse. The animal was imaged using the same protocol as described above at different time points as the lung-colonizing metastases appeared and progressed is size and number. The imaging time varied from 300 s/angular position for the first imaging sessions that were characterized by low bioluminescent signal, to 30 s/angular position for the later sessions when the bioluminescent signal was large. The average light output of these cells, as measured *in vitro*, was 58±6 photons/s/cell, significantly lower than the 198±10 photons/s/cell measured for the A549-LUC cells. MRI scans covering the chest of the mouse were acquired on a 4.7 T Varian system (Varian Inc. Palo Alto, CA 94304) using a custom built respiratory gating unit. We obtained contiguous spin-echo proton density weighted MR coronal slices (TE = 12 ms, FOV= 3.2 cm X 6.4 cm, slice thickness = 1 mm, matrix= 64 X 128 zero filled to 128 X 256, 4 averages). The LET images first detected a bioluminescent signal 22 days after cell implantation, and followed the growth and spread of the lung metastases at weekly intervals. Tumors in the lungs were first detected by MRI 46 days after

inoculations (see Fig. 5). The position and relative sizes of the tumors were consistent between the two imaging modalities. The smaller tumors from the left lung shown on the LET images were still not observed by MRI at that time, in agreement with the fact that even the visible tumors are not detected in the MR images taken 38 days after implantation.

Quantifying tumor volume

An important aspect of any imaging technique is the ability to quantify the property under study. Since assessing the tumor size is important in cancer studies, a comparison of the ability of planar BLI and the LET to quantify the size of tumors *in vivo* was performed. PC3-LUC cells injected in the flank of nude mice (BALBc/nu/nu) were imaged in the LETS using 5 second exposure time from 20 angular directions (5 positions x 4 cameras). The 0° angular view was used as a representative planar image and the total light emission was calculated and plotted against the volume calculated from caliper measurements of the tumors (Fig. 6a). Next, the tumors were reconstructed in 3D using the LET algorithm using 0.5 mm cubic voxels. Each tumor volume was estimated using the volume of the voxels exhibiting bioluminescence intensity above the background and compared with the caliper measurements (Fig. 6b). For small tumors the planar BLI yields good correlation with the caliper measurements (Fig. 6a), but when the larger tumors are considered the correlation worsens ($R^2 = 0.93$ versus $R^2 = 0.86$). Underestimation of the volume of large tumors by planar BLI

has also been reported by others [21]. The volume calculated using the 3D LET algorithm exhibits better correlation with the caliper measurements (R^2 = 0.988) and there is no degradation of the linearity for large tumors. Moreover, the linear regression has a zero intercept and a slope close to unity (0.925) indicating equivalence of the two measurements.

It should be mentioned that the experimental setup is ideal for planar imaging, since the tumors were close to the surface and very little light scattering and absorption is introduced by the overlaying tissues. In the case of tumors localized deeper in the animal the quantifying power of the planar BLI technique is expected to degrade significantly, and a 3D method such as LET may be expected to be superior.

DISCUSSION

We have demonstrated the feasibility of visualizing luciferase expressing cells at depth in a living mouse in 3D. The optical imaging system is based on high sensitivity cooled CCD cameras that rotate around the object and on an image reconstruction algorithm providing a three-dimensional reconstruction of the data in the multidirectional planar bioluminescence images. The method can provide not only volumetric, but also tomographic representations of the data. It also provides better quantification of the light emission than simple planar imaging techniques, as demonstrated in phantoms, thus enhancing the ability to assess and

monitor spatio-temporal characteristics of tumor growth, identifying metastases, and potentially determining the effectiveness of cancer treatment.

Since the technique is non-invasive, animals may be imaged for the entire course of an investigation, including tumor initiation, growth, treatment, and re-growth. Since the technique is highly quantitative, it permits accurate assessment of biological parameters using significantly fewer animals than previously possible. Beyond cancer, this methodology can be used to follow the fate of cells implanted at depth, such as stem cells.

To date, we have built a system using four cameras to acquire multiple images simultaneously, with additional rotation of the cameras to allow three-dimensional reconstruction . Clearly, additional cameras would provide increased sensitivity and provide better time resolution, thus enabling more effective studies of short-term dynamic processes.

The technique is capable of further increasing the usefulness of bioluminescence imaging, a modality which applies to many biological processes (*e.g.*, bacteria, tumor cells, immune cells, genes, *etc*.) tagged with reporter genes that encode several light-generating enzymes (luciferases) [22]. A significant advantage of bioluminescent assays *in vivo* is the inherent high signal to noise ratio, since host mammalian cells and tissues do not emit significant amounts of light [22, 23]. Reports have described detection of as few as 10^3 tumor cells in the peritoneal cavity, 10^4 cells at subcutaneous sites, 10^6 circulating cells immediately

following injection [24], and bone marrow metastases of approximately $2x10^4$ cells [6]. We were able to detect $5x10^3$ Mia-LUC cells orthotopically implanted in a mouse pancreas with signal/background ratio of 14 (Fig. 6c,d). The present study emphasizes the high sensitivity of the LET modality, providing the ability to locate specific cells in tissues and organs of living animals. LET facilitates monitoring the spatio-temporal distribution of bioluminescent tumor cells longitudinally during disease progression, and promises both qualitative and quantitative information, expanding the versatility and range of applications of bioluminescence imaging.

METHODS

High Sensitivity CCD camera

The imaging system uses CCD (charge-coupled device) cameras selected for their high and nearly constant sensitivity over the full range of wavelengths commonly used in optical imaging, from blue to near infrared. The CCD (SITe SI-032AB) is a non-color, back-illuminated, full frame image sensor with 512x512 pixels, (Scientific Imaging Technologies Inc., Tigard, OR). The quantum efficiency of the CCD is greater than 85% from 400 nm to 750 nm, and remains above 50% up to 900 nm. The CCD has a pixel size of 24x24 μm providing a large well capacity of 350,000 e^-, with a sensitivity of 2.6 μV/e^-, low dark current (20 pA/cm^2 at 20 ºC), and low readout noise (5 e^- RMS) providing a dynamic range of 75,000. The

CCD is cooled to -50° C reducing the dark current signal to less than 0.1 e^- /pixel/sec. The large dynamic range of the detector is coupled with a 16 bit analog to digital (A/D) converter, allowing quantitative detection of both high and very low signals, simultaneously, e.g. large tumors and nearby small metastases, or the proximal and distal views of the same tumor from opposite sides of the animal. This is a pivotal property for tomographic data acquisition, as the image intensity can vary by orders of magnitude as a function of the viewing angle. The CCD is incorporated in a self-contained, cooled camera, equipped with electronic circuitry and large aperture optics (25 mm focal length, f/0.95). Each camera is calibrated using a low-intensity, diffuse, flat field source that gives a known radiance (typically 3.0×10^{-7} W/cm^2/sr). The light source is periodically checked for uniformity using a NIST-traceable research radiometer (IL 1700, International Light, Inc. Newburyport, MA). By imaging this source the digital units provided by the camera digitizer can be converted directly into absolute physical units (W/cm^2/sr or photons/sec/cm^2/sr). Moreover, this method accounts for the transmission efficiency of the entire optical system, and corrects the field of view non-uniformity due to lens vignetting and variations in pixel sensitivity.

Camera sensitivity depends on several factors including object to image magnification factor (field of view dimensions for a given area of the CCD), f-stop, internal pixel binning, background signal, CCD temperature, and readout noise. As an example, we present an experiment in which 5×10^3 Mia-LUC cells

were injected into the pancreas of a BALBc/nu/nu mouse (Fig. 6c). After SQ injection of 450 mg/Kg luciferin an 8 minute image was acquired with 1x1 binning (highest resolution, but lowest sensitivity mode) and the maximum FOV (13.8 cm), i.e., the most difficult imaging conditions. Two representative regions of interest (ROI) were selected, one to determine the total signal from the implanted cells and the other to determine the background level. The signal/background ratio was 14, while the overall noise was less than 200 photons/sec/cm^2/sr. Thus, ~360 cells were required to produce a detectable signal, which corresponds to 2-5 cells per pixel, *in vivo,* for an S/N ~ 1.

Better sensitivity can be achieved by internally binning the signal from the adjacent pixels at the expense of resolution (2x2, 4x4, and 8x8 binning modes are software selectable). Smaller FOV would also give better sensitivity.

Multiple Head Optical Imaging System

Four high sensitivity CCD cameras simultaneously record views, and a computer controlled rotation mechanism allows imaging at multiple angular positions, required for three dimensional reconstructions. The support electronics allow simultaneous control of the cameras for light exposure, image readout and preprocessing, and temperature and vacuum control. Since each camera in the system is calibrated in absolute units all resulting images can be directly combined by the reconstruction algorithm. A horizontal bed, made of sparse mesh material to reduce interference with light, is used to support and immobilize the

animal during imaging. A gas anesthesia unit is connected to the bed and to the animal. While a four camera system has been designed and built, some of the reported data were acquired with just two cameras and additional rotations. To exclude ambient light, the system is encapsulated in a light-tight enclosure. Light images at each position of the gantry are acquired for co-registration with the bioluminescence image using a set of 6 diffuse light sources.

Image Reconstruction Software

Optical imaging methods are subject to the complexity of light transport and practical, high-resolution 3D image reconstruction algorithms for bioluminescence or continuous-wave source imaging have been lacking. Some initial attempts at depth determination have been reported [25].

In general, the image reconstruction problem has been approached in two limiting cases. For single-scattered light, as described by the first-order Born or Rytov approximation, depth-resolved microscopic methods (multi-photon fluorescence and confocal reflectance) are limited in depth to several hundred microns. In optical coherence tomography, this depth localization can be increased to ~2.5 mm using coherent light sources [26]. At the opposite extreme, light that scatters many times during propagation has been modeled extensively using the diffusion approximation to the Boltzmann transport equation. Prototype systems for optical transmission tomography of the breast and brain exist [27, 28], and image reconstruction algorithms analogous to traditional filtered

backprojection and filtered backpropagation for diffraction tomography have been proposed [29, 30]. Application of the diffusion approximation has been described for planar *in vivo* imaging with light-emitting probes [11], but algorithms for light emission tomography have lagged behind developments for optical transmission tomography [31]. Good results for 3D optical reconstruction have also been obtained by using the Finite Element Method (FEM) and multispectral imaging in simple phantoms [16, 32].

We have developed a novel 3-D reconstruction algorithm for small animal imaging, and this paper presents the results for reconstruction in the multi-scattering, continuous wave regime. Our reconstruction approach consists of two steps: light surface reconstruction to determine geometry of turbid media boundary and then source reconstruction inside the tissue by using a deblurring EM algorithm based on diffusion equations as described by Slavine *et al* [19].

The 3D surface reconstruction is based on a Maximum Likelihood Expectation Maximization method (MLEM) [33]. Using the MLEM algorithm, a sequence of image estimates is generated for the k^{th} iteration:

$$n_j^{k+1} = \frac{n_j^k}{\sum_{i=1}^{I} a_{ij}} \sum_{i=1}^{I} \frac{m_i}{q_i^k} \qquad \text{where} \qquad q_i^k = \sum_{j=1}^{J} a_{ij} n_j^k \qquad (1)$$

where n_j^{k+1} and n_j^k are image intensity values in the new and current estimate for the voxel j. The measured data m_i collected along the i^{th} lines of response

(LOR_i), which came from the surface to the CCD camera and being proportional to the light intensity detected by the pixel; q_i^k is the expected count in LOR *i* for the current estimate n^k, and a_{ij} is the probability that a light quantum emitted at voxel *j* will be detected in the LOR_i. The normalization factor $\sum_{i=1}^{I} a_{ij}$ includes all possible measured LOR's.

For source reconstruction inside the tissue we apply the following algorithm:

1. In order to estimate the source location we backproject our experimental data into the volume discretized into $N_x \times N_y \times N_z$ voxels. In this step we obtain estimations for X, Y and Z coordinates of all light sources in the reconstructed volume.

2. Calculate the intensity of reflection on boundary for each voxel *j* , and subtract its contribution from the transmitted part of intensity recorded by the CCD. The diffusion equation is used to determine the balance intensities for internal sources N_s for the surface element in a single voxel (see [19] and references therein).

3. For each voxel *j* we can determine a "zero-th" order approximation φ_j^0 using the solution for photon fluence:

$$\varphi_j^0 = (\rho \otimes \varphi + \hat{n})_j \cong \frac{1}{\sum_{i=1}^{I} x_{ij}\, p_i^t} \sum_{i=1}^{I} x_{ij}\, p_i^0 \sum_{s=1}^{s=N_s} S_o^{'}\ \exp(-\mu_{eff}\, r_{js}) / r_{js} \qquad (2)$$

where ρ is a point-spread function, φ is a real value of photon fluence, $\hat{n}$ is a noise term, and x_{ij} is the path length of line i through voxel j, p_i^t and p_i^0 are intensities in CCDs from source in media and in air. Here, we utilized the basic function from the semi-infinite geometry as a first approximation to the diffuse photon propagator.

4. Apply the deblurring EM algorithm [34] for final 3D-image reconstruction by using approximation (2)

$$\varphi_j^{n+1} = \varphi_j^n \left\{ \hat{\rho} \otimes \left(\frac{\varphi_j^0}{\rho \otimes \varphi_j^n} \right) \right\} \qquad (3)$$

where $\otimes$ denotes convolution procedure based on the discrete Fast Fourier Transform (FFT). Parameters ρ and $\hat{\rho}$ are the deblurring kernels (for example Gaussian functions) and can be changed with number of iterations n.

We focus here on whole body imaging with a typical reconstruction volume of 100 x 60 x 60 mm. Data acquisition using a single camera lasts 15 - 40 minutes, with four cameras 5 - 10 minutes depending on the required exposure time. With a voxel dimension of 0.5 mm, the reconstruction takes approx. 2 hrs. With these typical choices, the S/N ratio for each individual view (individual *in vivo* planar image used for the 3D reconstruction) is in the range of 15 - 60. After

three-dimensional reconstruction, the measured S/N ratio increases significantly to 1 - 2 x 10^3. This reflects the noise handling ability found in other MLEM based applications. In the context of these choices, the resolution for bioluminescence sources at a depth of 5 mm in tissue like material was 1.5-2 mm.

Acknowledgements

We are grateful to Trung Nguyen, Billy Smith, Allen Harper, and Drs. G.M. Arbique and A. Zinchenko for assistance with technical development. This work was supported in part by funds from the Simmons Cancer Center, the UT Southwestern/MD Anderson Lung SPORE CA70907, the Cancer Imaging Program P20 (Pre-ICMIC) CA 86354, and DOD Breast Cancer Initiative W81XWH-04-1-0551.

References

1. Contag, C.H. & Ross, B.D. It's not just about anatomy: in vivo bioluminescence imaging as an eyepiece into biology. *J. Magn. Reson. Imaging* **16**, 378-387. (2002).
2. Marx, J. Animal Models: Live and in Color. *Science* **302**, 1880-1882 (2003).
3. Herschman, H.R. Molecular imaging: looking at problems, seeing solutions. *Science* **302**, 605-608 (2003).

4. Hardy, J. et al. Extracellular replication of Listeria monocytogenes in the murine gall bladder. *Science* **303**, 851-853 (2004).

5. Vooijs, M., Jonkers, J., Lyons, S. & Berns, A. Noninvasive imaging of spontaneous retinoblastoma pathway-dependent tumors in mice. *Cancer Res.* **62**, 1862-1867. (2002).

6. Wetterwald, A. et al. Optical imaging of cancer metastasis to bone marrow: a mouse model of minimal residual disease. *Am. J. Pathol.* **160**, 1143-1153 (2002).

7. Burgos, J.S. et al. Time course of bioluminescent signal in orthotopic and heterotopic brain tumors in nude mice. *Biotechniques* **34**, 1184-1188 (2003).

8. Wu, J.C. et al. Molecular imaging of cardiac cell transplantation in living animals using optical bioluminescence and positron emission tomography. *Circulation* **108**, 1302-1305 (2003).

9. Paroo, Z. et al. Validating bioluminescence imaging as a high-throughput, quantitative modality for assesing tumor burden. *Mol. Imaging* **3**, 117-124 (2004).

10. Massoud, T.F. & Gambhir, S.S. Molecular imaging in living subjects: seeing fundamental biological processes in a new light. *Genes Dev.* **17**, 545-580 (2003).

11. Rice, B.W., Cable, M.D. & Nelson, M.B. In vivo imaging of light-emitting probes. *J. Biomed. Opt.* **6**, 432-440. (2001).

12. Tromberg, B.J. et al. Non-invasive in vivo characterization of breast tumors using photon migration spectroscopy. *Neoplasia* **2**, 26-40 (2000).

13. Weissleder, R., Tung, C.H., Mahmood, U. & Bogdanov, A., Jr. In vivo imaging of tumors with protease-activated near-infrared fluorescent probes. *Nat. Biotechnol.* **17**, 375-378. (1999).

14. Ntziachristos, V., Ripoll, J., Wang, L.V. & Weissleder, R. Looking and listening to light: the evolution of whole-body photonic imaging. *Nat. Biotechnol.* **23**, 313-320 (2005).

15. Troy, T.L., Stearns, D.G., Nilson, D.N. & Rice, B.W. in Advances in Optical Imaging and Photon Migration 513-515 (Optical Society of America, Miami Beach, Florida; 2002).

16. Gu, X., Zhang, Q., Larcom, L. & Jiang, H. Three-dimensional bioluminescence tomography with model-based reconstruction. *Opt. Express* **12**, 3996 - 4000 (2004).

17. Chaudhari, A.J. et al. Hyperspectral and multispectral bioluminescence optical tomography for small animal imaging. *Phys Med Biol* **50**, 5421-5441 (2005).

18. Alexandrakis, G., Rannou, F.R. & Chatziioannou, A.F. Tomographic bioluminescence imaging by use of a combined optical-PET (OPET)

system: a computer simulation feasibility study. *Phys Med Biol* **50**, 4225-4241 (2005).

19. Slavine, N.V., Lewis, M.A., Richer, E. & Antich, P.P. Iterative reconstruction method for light emitting sources based on the diffusion equation. *Med Phys* **33**, 61-68 (2006).

20. Firbank, M., Oda, M. & Delpy, D.T. An improved design for a stable and reproducible phantom material for use in near-infrared spectroscopy and imaging. *Phys. Med. Biol.* **40**, 955-961 (1995).

21. Sarraf-Yazdi, S., Mi, J., Dewhirst, M.W. & Clary, B.M. Use of in vivo bioluminescence imaging to predict hepatic tumor burden in mice. *J. Surg. Res.* **120**, 249-255 (2004).

22. Contag, C.H. & Bachmann, M.H. Advances in in vivo bioluminescence imaging of gene expression. *Annu. Rev. Biomed. Eng.* **4**, 235-260 (2002).

23. Mandl, S., Schimmelpfennig, C., Edinger, M., Negrin, R.S. & Contag, C.H. Understanding immune cell trafficking patterns via in vivo bioluminescence imaging. *J. Cell Biochem. Suppl.* **39**, 239-248. (2002).

24. Edinger, M. et al. Noninvasive assessment of tumor cell proliferation in animal models. *Neoplasia* **1**, 303-310. (1999).

25. Coquoz, O., Troy, T.L., Jekic-MsMullen, D. & Rice, B.W. Determination of depth of *in-vivo* bioluminescent signals using spectral imaging techniques. *Proc. SPIE* **4967**, 37-45 (2003).

26. Huang, D. et al. Optical Coherence Tomography. *Science* **254**, 1178-1181 (1991).

27. Colak, S.B. et al. Tomographic image reconstruction from optical projections in light diffusing media. *Appl. Opt.* **36**, 180-213 (1997).

28. Jiang, H. et al. Three-Dimensional Optical Tomographic Imaging of Breast in A Human Subject. *IEEE Trans. Med. Imaging* **20**, 1334-1340 (2001).

29. Dorn, O. A transport-backtransport method in optical tomography. *Inverse Probl.* **14**, 1107-1130 (1998).

30. Matson, C.L. & Liu, H. Backpropagation in turbid media. *J. Opt. Soc. Am. A.* **16**, 1254-1265 (1999).

31. Ntziachristos, V. & Weissleder, R. Experimental three-dimensional fluorescence reconstruction of diffuse media by use of a normalized Born approximation. *Opt. Lett.* **26**, 893-895 (2001).

32. Cong, A.X. & Wang, G. Multispectral Bioluminescence Tomography: Methodology and Simulation. *International Journal of Biomedical Imaging*, 1-7 (2006).

33. Shepp, L.A. & Vardi, Y. Maximum likelihood reconstruction for emission tomography. *IEEE Trans. Med. Imaging* **1**, 113-122 (1982).

34. Jiang, M., Wang, G., Skinner, M.W., Rubinstein, J.T. & Vannier, M.W. Blind deblurring of spiral CT images. *IEEE Trans. Med. Imaging* **22**, 837-845 (2003).

Supplementary Material

Supplementary Movie S1

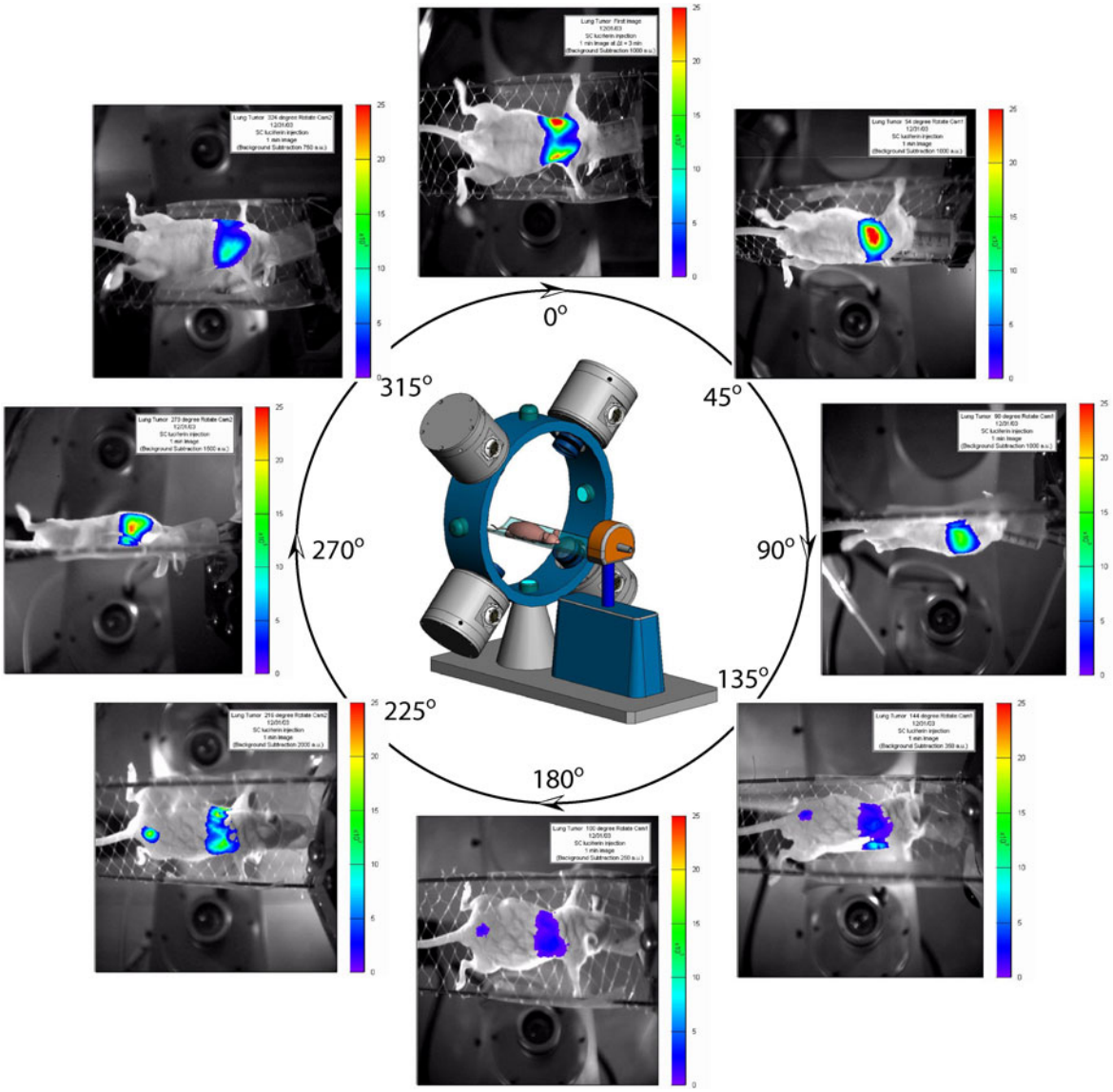

Figure 1. A selection of eight planar images obtained from specified angles showing bioluminescent signal overlaid on photographs of illuminated mouse. The nude mouse was implanted with A549-LUC human tumor cells. In total 20 images were acquired for the 3-D reconstruction shown in Figure 4.

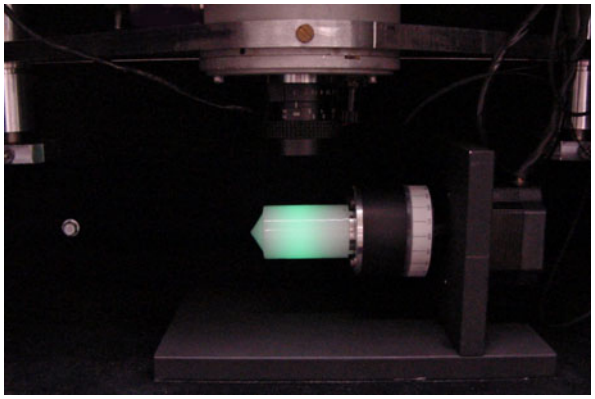

a

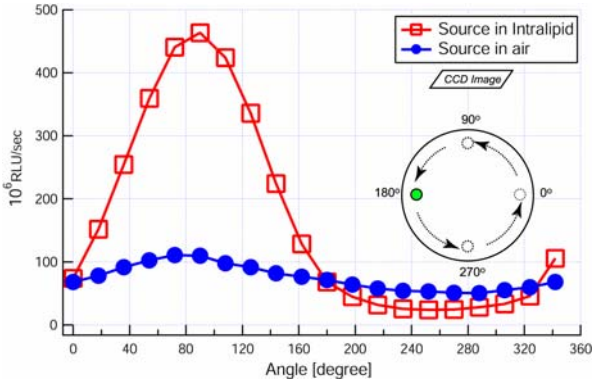

b

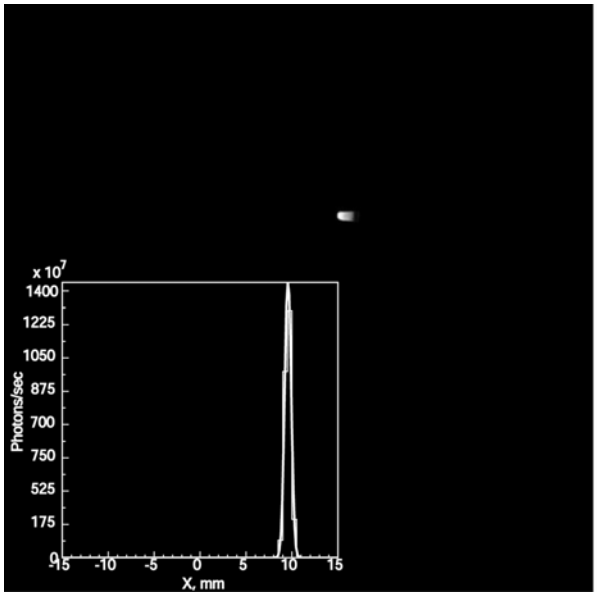

c

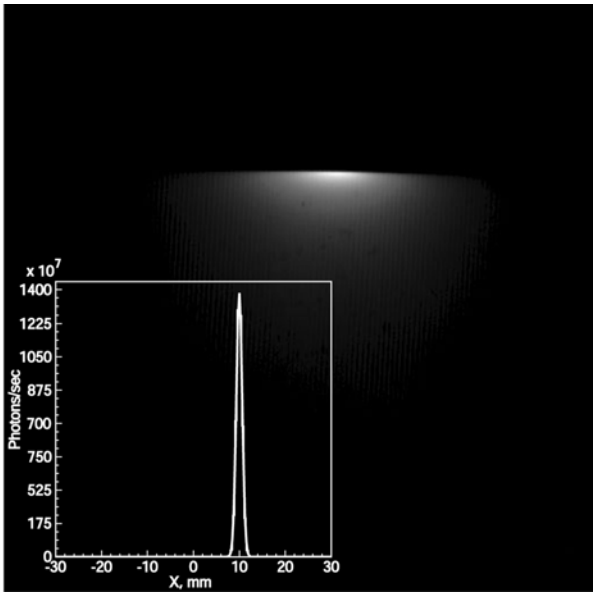

d

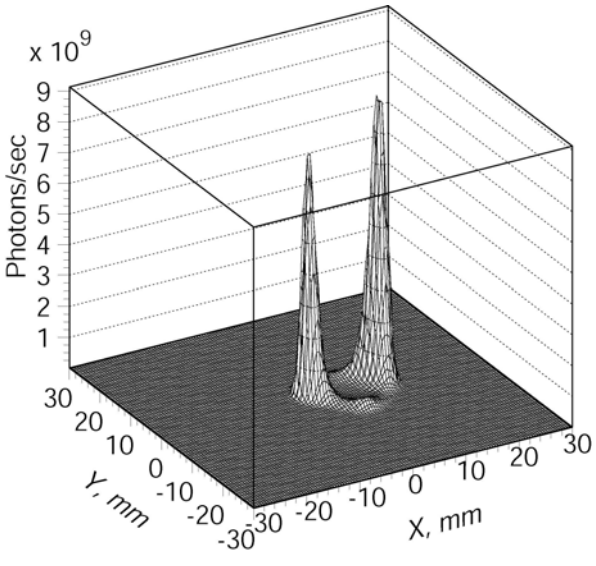

e

Figure 2. Validation of LET in phantoms.

a. Experimental setup: 30 mm cylindrical phantom filled with 1% Intralipid gel.

b. Total amount of light captured from a fiber optic source in air and in the Intralipid phantom at various angles. The light source is displaced 10 mm from the axis of rotation.

c, d. Image of light emitting fiber in air (c) and in Intralipid-filled medium (d) displaced 10 mm from the center. The intensity profiles through the reconstructed 3D image are also shown.

e. 3D intensity profiles for 1% Intralipid phantom with two sources separated by 10 mm.

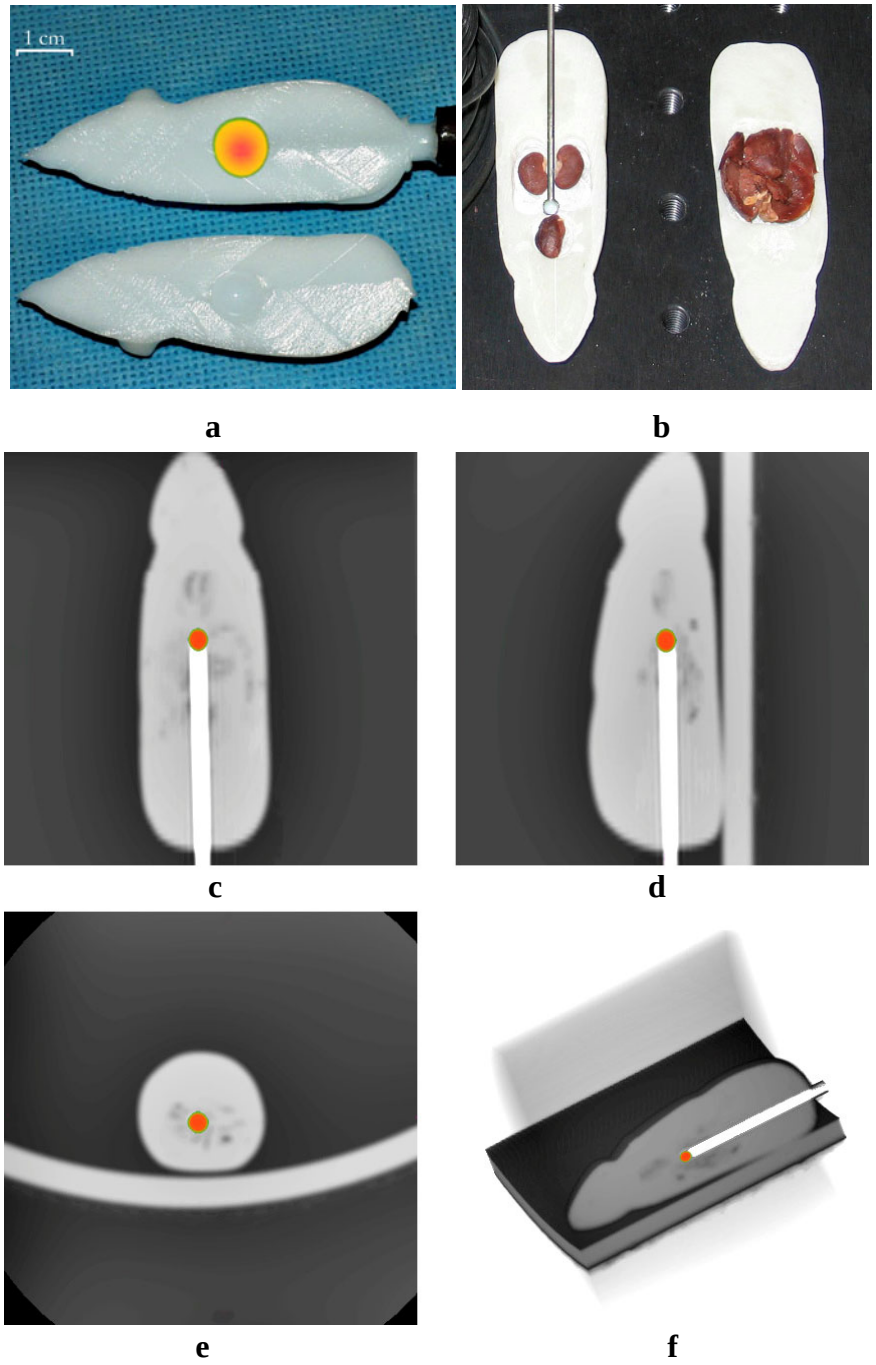

Figure 3. a. Homogeneous mouse shaped Intralipid gel phantom, sectioned after imaging, showing the 9.5 mm spherical light source and the 3D reconstruction overlay.

b. Heterogeneous mouse shaped phantom with tissue like optical properties (μ_a = 0.3 cm^{-1}, μ_s' = 9 cm^{-1}), and formalin fixed mouse organs. 3 mm light source placed between heart and liver.

c, d e, f. Co-registered CT (imaged with GE CT/I, 3D reconstruction using VolView 2.0, Kitware, Inc), and LET 3D image.

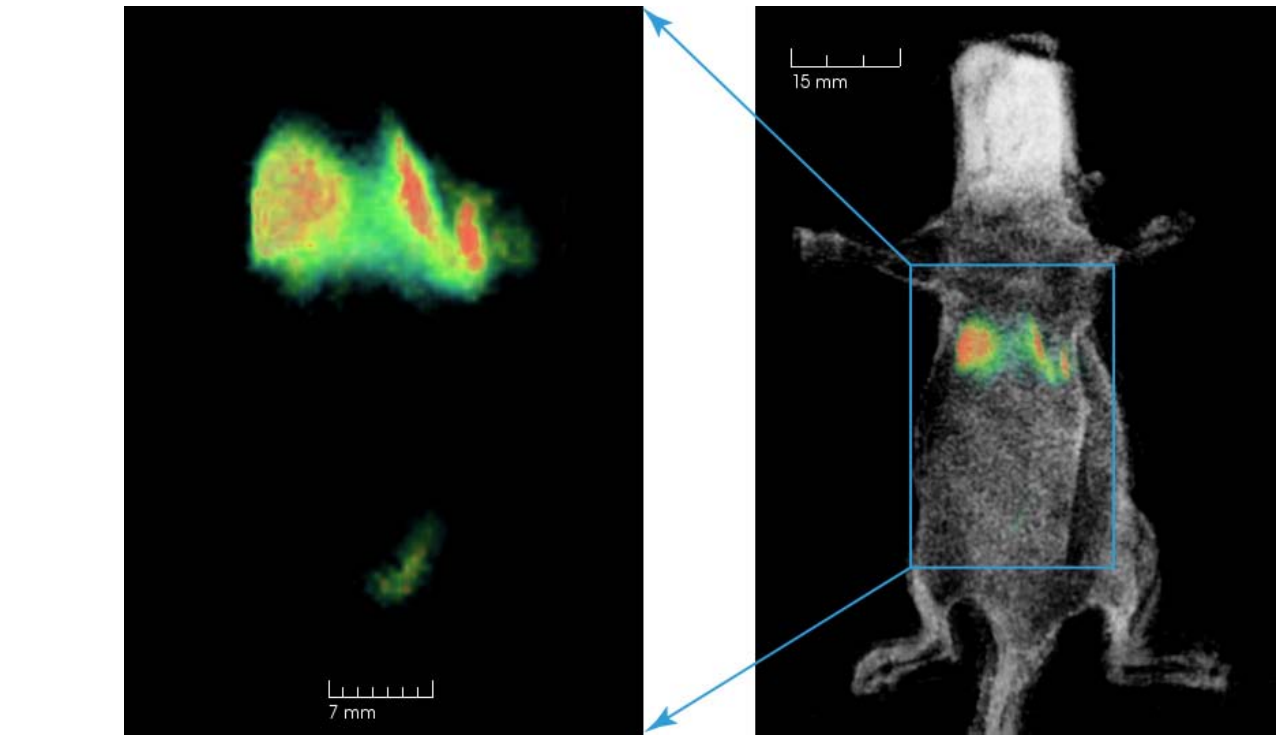

a **b**

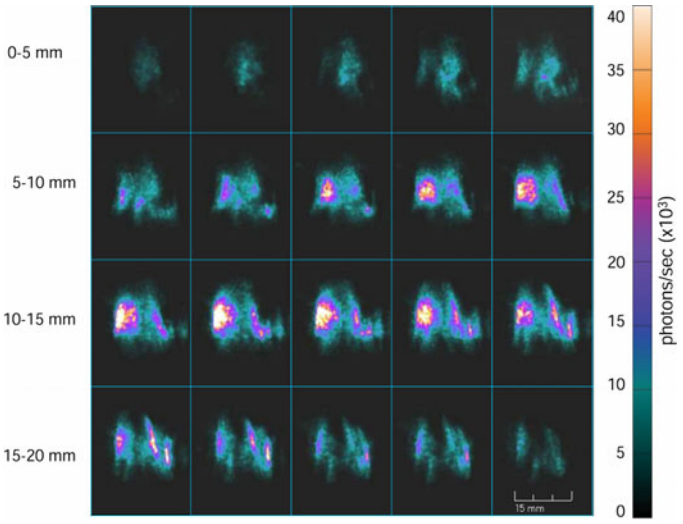

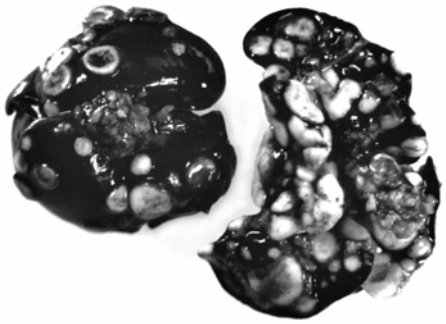

c **d**

Figure 4. a. 3-D reconstruction of bioluminescence and **(b)** overlay on surface reconstruction from external light images. The anesthesia mask is seen over the nose of the mouse in the reflected light image. (Note: the images are at different scales.)

c. Coronal cross-sections of bioluminescent data showing A549-LUC tumors in mouse lungs. The sections are 0.5 mm thick, 1 mm apart, and start dorsally (top left corner) ending ventrally (bottom right).

d. Staining of intact lungs by injection of India ink directly into the trachea indicates approximately 10^3 metastatic foci.

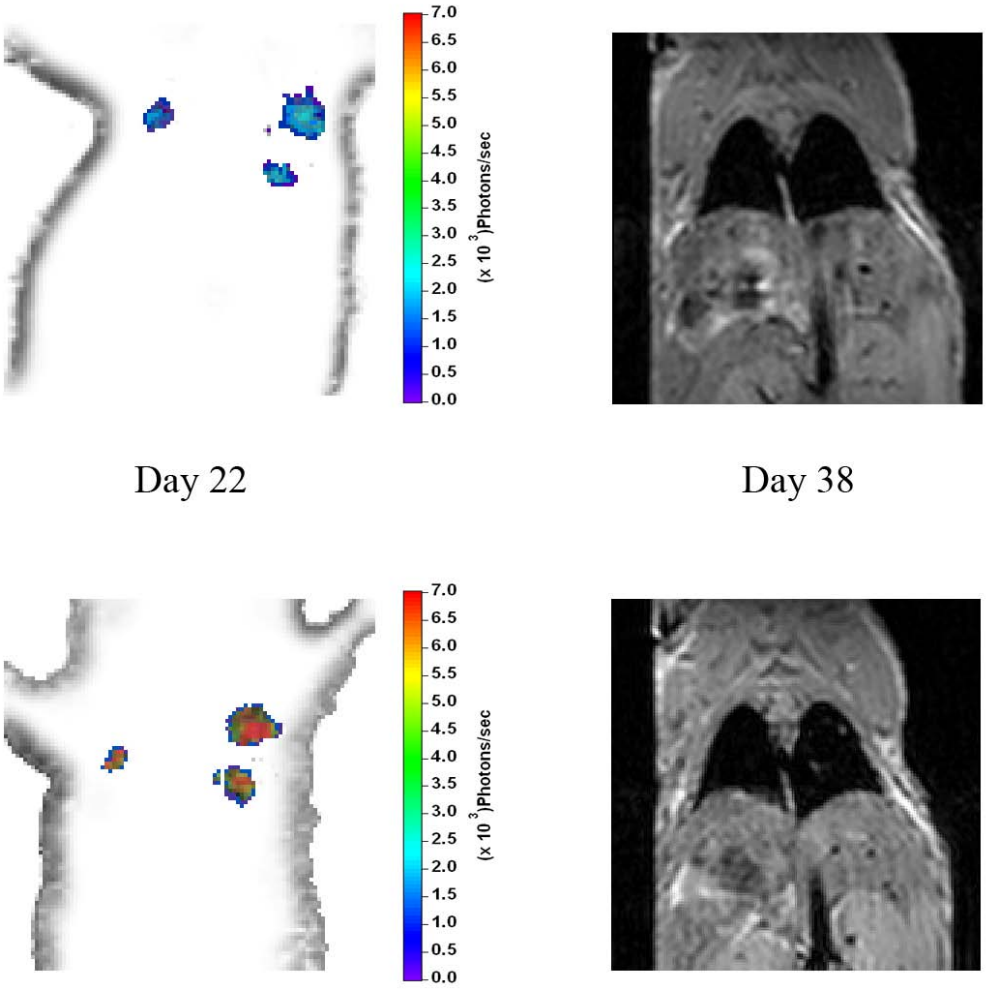

Figure 5. Comparison of LET and MRI taken at different time points in MDA-MB-231-LUC lung metastases model. Coronal slices are 1 mm thick and they correspond to the same position in the animal. LET was capable to correctly localize the tumors, and detected them 17 days earlier. MRI did not detect the smaller tumor in the left lung. MR images were obtained with a 4.7 T Varian scanner.

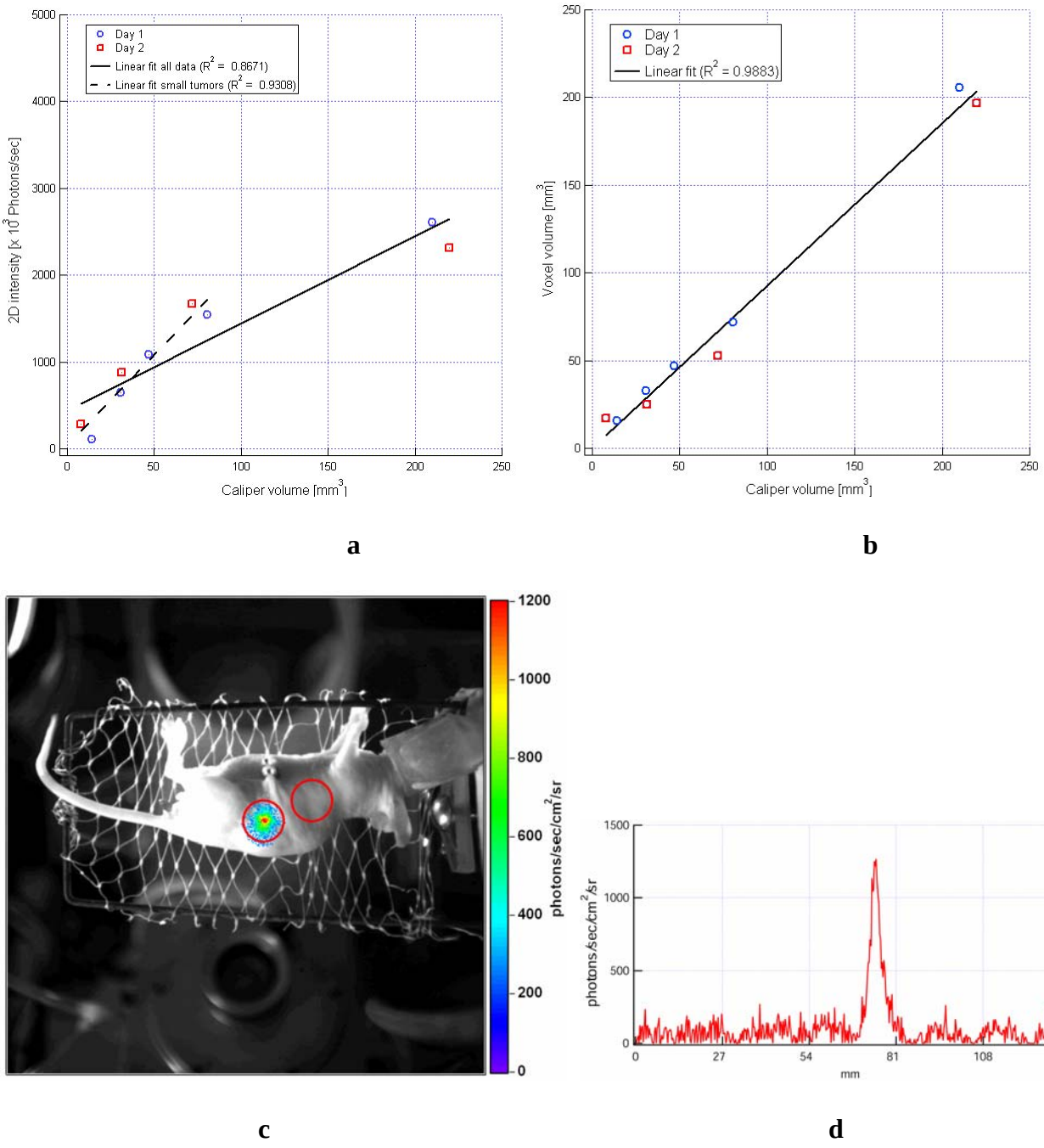

Figure 6. a. Correlation of the planar bioluminescence and **(b)** of 3D LET reconstructed volume with caliper measurements.

c. Image of $5x10^3$ Mia-LUC cells injected in the pancreas of a BALBc/nu/nu mouse. Circles indicate the ROI for S/N calculation.

d. Cross section profile of the bioluminescent signal.